Università di Pisa

FACOLTÀ DI SCIENZE MATEMATICHE, FISICHE E NATURALI
Corso di Laurea in Fisica Teorica

Faint progenitors of luminous quasars: where are they?

Tesi di Laurea in Fisica

Relatore:
Chiar.mo Prof.
Andrea Ferrara

Co-relatrice:
Dott.
Simona Gallerani

Presentata da:
Maria Carmela Orofino

Anno Accademico 2014-2015

Contents

Abstract

We studied the visibility of the supermassive black holes' ancestors in the X-ray band. Our goal was to assess if their detection is at reach of the current observational capabilities.

We used the results of a semi-numerical simulation to evaluate the X-ray emission of the progenitors, taking into account the attenuation processes that occurs as the radiation travels through the interstellar medium of the host galaxy. Then we compared our results with the sensitivity of the most powerful observatory available, the Chandra Space Telescope, finding that the expected emission is strong enough to be revealed, although these objects are too rare to be detected with the past surveys.

Accounting for the technical difficulties that arise in performing a survey, we planned the best observational strategy to maximize the detection probability. We found that is more advantageous for a survey to explore an area as large as possible to the detriment of the sensitivity. These results are encouraging because none of the past surveys implemented the optimal strategy and therefore there is ample room for improvement: even if they have not been detected so far, we expect the detection to be possible in the near future.

1 Introduction

Structure formation in the early universe is one of the most interesting and wide-spreading research field in cosmology. The detection of the Cosmic Microwave Background suggests that four-hundred-thousand years after the Big Bang our universe was almost homogeneous, with tiny density fluctuations ($\frac{\delta\rho}{\rho} \sim 10^{-5}$). Such fluctuations, due to gravitational instabilities, collapsed forming the large scale structures that we can observe in the local Universe.

Using the most powerful observatories, we have been able to observe objects at $z \sim 7-8$, namely a little more than 650 million years after the Big Bang. In addition to the primordial galaxies, we also find quasars, sources powered by Super Massive Black Holes (SMBHs). Currently, the most distant quasar known has a redshift $z \sim 7$ (corresponding to less than one billion years after the Big Bang) and is powered by a SMBH of $M \sim 10^9 M_\odot$.

The formation of such massive objects is one of the most fascinating open problems in cosmology. The first outstanding issues concerns the nature of SMBHs' seeds: they could be stellar-mass BHs, formed by remnants of massive stars, or heavier structures with intermediate mass ($10^{4-5} M_\odot$), perhaps formed by direct gravitational collapse. The second concerns the growth of BHs' seeds either by the accreting material falling into the black hole or by merging. So far, several attempts have be done in order to detect SMBHs' ancestors: in fact, BHs' environments are the brightest objects in the Universe. The accreting material spirals towards the BH, heating by viscous rubbing against itself and shining with an extremely efficient process (more than the 10 percent of the gas mass is converted into heat). Unlike, stellar-objects they present a strong emission in the X-rays band; so that a possible strategy to detect them is to observe the sky in this band. It has been done with the most powerful tool available at the moment, the Chandra X-ray Observatory Satellite, but we have not got any positive response at the present time.

The aim of our thesis is to investigate the possible causes that could have hidden SMBHs' ancestors from our surveys. In particular we will consider two main hypothesis:

- SMBHs' ancestors are obscured, being buried in significant amounts of gas and dust that absorb most of the outflowing radiation.
- They are too rare to have been detected in the volume investigated by the past surveys, hence they are statistically not observed.

For our purpose, we will use the results of a semi-numerical simulation that provides us details on the SMBHs' progenitors accretion and on the amount of obscuring material in their environs. Hence, combining the numerical results with the current observational data, we will compute the ancestors' expected X-ray spectrum, including several interstellar absorption processes. We will find that the predicted X-ray emission is highly suppressed in the soft band ($[0.5 \div 2]$ keV) and almost unobscured in the hard one ($[2 \div 10]$ keV).

The expected X-ray flux is well in reach of the most powerful current observatories: hence the reasons for the non-detection are due to the rarity of these sources and to the limited area probed by the latest deep surveys. To investigate this issue, in the final part of the thesis we will develop a formalism to obtain, given the characteristics of the survey, how many sources are supposed to be detected.

This work is organised as follows:

- **Chapter 2**: it is an introduction that illustrates the standard cosmological model and the basic tools needed to study structure formation.
- **Chapter 3**: here we consider the physics of the brightest objects in the universe, the *active galactic nuclei* (AGNs), exploring the nature of their central engine.
- **Chapter 4**: here we introduce the scientific issue related to the AGNs formation and present some of the most accredited theoretical model developed to solve it.
- **Chapter 5**: in this chapter we present our analytical model for the AGNs' X-ray emission, involving several attenuation processes.
- **Chapter 6**: we analyze the observational forecasts of the previous estimates and perform a statistical analysis to determine a best observational strategy.
- **Chapter 7**: we conclude with brief summary of the work done and the results obtained, considering the limitation of our works and the prospects for the near future.

2 Cosmological Background

This chapter is a brief introduction to cosmology, needed to contextualize our work: here we will present the main feature of the cosmological standard model and the background necessary to study the formation of structures in our universe.

In section 2.1, our starting point will be the *cosmological principle*, which the whole modern cosmology is based on, together with the observational patency that the universe is expanding. Then, in section 2.2 we will present the model currently used to describe the formation of the large scale structures that we observe in our universe, handling with the collapse of gravitational instabilities.

2.1 The expanding Universe

In 1929, Erwin Hubble inferred from observations that distant galaxies are receding from us with a velocity that is proportional to their distance:

$$v = H_0 d, \tag{2.1}$$

where the quantity H_0 is called *Hubble constant*. The meaning of the previous equation, known as *Hubble law*, is well explained in the context of General Relativity, that relates the geometry of the universe to its matter content.

In this section, we will describe the kinematics (sec. 2.1.1) and the dynamics (sec. 2.1.2) of the universe, assuming that it is homogeneous and isotropic (approximation that is excellent on large scales but obviously fails on small ones), preparing the ground for the contextualization of this work.

2.1.1 The cosmological principle

All the modern cosmology is based on the statement that, at *any* epoch, the universe appears *the same* to *all* observers, regardless their individual locations. This statement, known as *the cosmological principle*, is basically a generalisation of the Copernican principle and is equivalent to say that the universe is homogeneous and isotropic.

In general relativity, there are only three metrics that describe a homogeneous and isotropic universe: the Robertson and Walker metrics,

$$ds^2 = c^2dt^2 - a^2(t)\left(\frac{dx^2}{1-kx^2} + x^2(d\theta^2 + \sin^2\theta d\phi^2)\right) \tag{2.2}$$

where $a(t)$ is an overall scale factor that describes the expansion of the spatial coordinates in time and k is the scalar curvature that determines the geometry of the space and can takes values -1 (corresponding to an open universe), 0 (flat), +1 (close). However, current observations support the statement that the universe is flat and in this work we will consider $k = 0$.

Equation (2.2) uses *comoving* coordinates: the universe expands as $a(t)$ increases but observers keeps fixed the coordinates x, θ, ϕ as long as there are not forces acting on them, condition that is called "absence of peculiar motion". The corresponding physical (or *proper*) coordinates is $r(t) = a(t)x$ and is time dependent even in absence of peculiar motion.

The main information that can be extracted from the metric (2.2) concerns the propagation of light. Consider a light ray emitted by a source at a time t_e and received by an observer at a time t_o; light rays are characterized by null geodesics ($ds^2 = 0$), that means $cdt = -a(t)dx$, where the sign - accounts for the fact that the light is travelling towards the observer.

The separation between the wave fronts is Δt_e at the emission and Δt_o at the detection, but the distance x travelled by the fronts must be constant:

$$x = \int dx = -\int_{t_e}^{t_o} \frac{cdt}{a(t)} = -\int_{t_e+\Delta t_e}^{t_o+\Delta t_o} \frac{cdt}{a(t)}, \tag{2.3}$$

that means:

$$\frac{\Delta t_o}{a(t_o)} = \frac{\Delta t_e}{a(t_e)} \tag{2.4}$$

and

$$\frac{a(t_o)}{a(t_e)} = \frac{\Delta t_o}{\Delta t_e} = \frac{\nu_e}{\nu_o} = 1 + z \tag{2.5}$$

where ν is the frequency of the electromagnetic wave and the redshift z is defined by $z = \frac{\nu_e - \nu_o}{\nu_o}$. Eq. (2.5) suggests that the redshift z can be interpreted as a measure of the size of the universe at emission with respect to the present: for example, at $z = 1$ the universe was an half of the universe today.

From equation (2.5), knowing the time dependence of the scale factor $a(t)$, we can convert the redshift z of a source in a time coordinate: setting $t_o = t_0$, where the label "0" means "at the present time", and $t_e = t$, the radiation emitted by a source that present a redshift z was emitted at time t in the past.

Before to deal with the time dependence of the scale factor (see subsection 2.1.2), it is interesting to point out some observations. First of all, the Hubble law (2.1) tell us that the velocity at which a galaxy is moving away from us is proportional to its distance from us: $v_i = H_0 r_i$, where the index i refers to the galaxy that we are observing.

We can express velocity as the time derivative of the proper distance:

$$v_i = \frac{dr_i}{dt} = x_i \dot{a}(t)|_{t=0} = r_i \frac{\dot{a}(t_0)}{a(t_0)}, \tag{2.6}$$

that compared with the Hubble law gives $H_0 = \frac{\dot{a}(t_0)}{a(t_0)}$ or in general:

$$H = \frac{\dot{a}(t)}{a(t)}. \tag{2.7}$$

Another important reflection concerns the apparent intensity of a light source. We know that the luminosity (i.e. the power) emitted by a source is affected by a dilution due to its distance from the observer. But, since the universe is expanding, the expression for the flux deviate from the usual $\frac{1}{x^2}$ dependence.

Considering a source at a comoving distance x from us is characterized by a bolometric luminosity L (i.e. the power emitted over the whole spectrum), we have to take into account that:

- The geometry of the space-time modifies fluxes. Nevertheless, we have already highlighted that current observations support a flat universe, hence the surface area involved in the calculation of the flux is the euclidean $4\pi x^2$.
- The energy of the emitted photons is redshifting while travelling to us:

$$h_p \nu_0 = \frac{h_p \nu_e}{1+z}. \tag{2.8}$$

- The arrival rate of the photons is stretched by $(1+z)$.

These statements mean that, for example, if a source at $z = 9$ from us emits 10 photons of energy 10 keV for unit time, we will receive 1 photons of 1 eV in the same time interval.

Thus the bolometric flux is:

$$f_{bol} = \frac{L}{4\pi x^2 (1+z)^2} = \frac{L}{4\pi d_L^2} \tag{2.9}$$

where d_L is known as *luminosity distance*.

Is worth to notice that if we consider a monocromatic flux f_ν instead to bolometric one, it is:

$$f_{\nu_0} = \frac{L_{\nu_e}(1+z)}{4\pi d_L^2}, \tag{2.10}$$

due to the redshifting of the considered frequency.

Another important observation concerns the angular size of a source at redshift z. Due to the expansion of the universe, the angle θ under which we see a source is increased of a factor $(1+z)$:

$$\theta = \frac{S(1+z)}{x} = \frac{S}{D_\theta}, \tag{2.11}$$

where S is the proper diameter of the source and D_θ is the *angular size distance*.

Hence, as a consequence of the expansion of the universe, astronomical objects appear less luminous but larger. Luminosity distance and angular size distance are related to each other by: $d_L = (1+z)^2 D_\theta$.

2.1.2 The Friedmann equations

In order to understand the time dependence of the scale factor $a(t)$ and the evolution of the universe, known the fluids it is composed of, we need to exploit the general relativity and the conservation laws. The main results of general relativity are Einstein equations:

$$R_{\mu\nu} - \frac{1}{2} g_{\mu\nu} R = \frac{8\pi G}{c^4} T_{\mu\nu} \tag{2.12}$$

that, read left-to-right mean that geometry of the space-time is affected by matter and read right-to-left mean that fixed the geometry, it determines how the matter moves.

It can be demonstrated that, due to the fact the Robertson and Walker metric (eq. (2.2)) is particularly simple (with the hypothesis of homogeneity and isotropy), the eqs. (2.12) give only two independent equations, the Friedmann equations:

$$H^2 = \left(\frac{\dot{a}(t)}{a(t)}\right)^2 = \frac{8\pi G}{3}\rho - \frac{kc^2}{a(t)} \tag{2.13}$$

$$\ddot{a}(t) = -\frac{4\pi G}{3} a(t) \left(\rho + \frac{3P}{c^2}\right) \tag{2.14}$$

that express the evolution of the universe in terms of the scale factor. It is important to notice that there is a *critical density* ρ_c for which the universe is flat

$(k = 0)$:

$$\rho_c = \frac{3H^2}{8\pi G} \tag{2.15}$$

a universe with $\rho > \rho_c$ would be closed $(k > 0)$, one with $\rho < \rho_c$ would be open $(k < 0)$.

Since for homogeneity and isotropy there cannot be any heat transfer, the energy conservation is:

$$c^2 d(\rho V) = -P dV, \tag{2.16}$$

that, considered a volume $V = V_0 a^3(t)$, and a simple equation of state $P(\rho) = wc^2\rho$, yields:

$$\frac{d\rho}{\rho} = -3(1+w)\frac{da}{a} \Longrightarrow \rho \propto a^{-3(1+w)}. \tag{2.17}$$

In the '90s, took root the standard model of cosmology, known as ΛCDM, that introduces an exotic fluid (the *Dark Energy*) to solve the issue derived from the experimental patency that the universe is accelerating.

According to the ΛCDM model, the density of the universe is made up by four components:

- *Baryonic matter* - This component contains both baryons and leptons (without neutrinos) and, according to the new Planck collaboration release (Planck Collaboration et al. 2015), is the 4.9% of the total. In the redshift range of our interest the baryonic matter is not relativistic, hence its pressure is negligible $(w = 0)$ and eq. (2.17) yields:

  $$\rho_b(z) = \rho_{b,0}(1+z)^3, \tag{2.18}$$

  as it is intuitive since the density of the ordinary matter is diluted by the expansion of the universe.

- *Radiation and relativistic matter* - This fluid consists in photons and neutrinos and at the present time its density is $\approx 10^{-5}\rho_{tot}$. For radiation $P = \rho/3$ and eq. (2.17) gives:

  $$\rho_r(z) = \rho_{r,0}(1+z)^4, \tag{2.19}$$

  as expected, since the photons are both redshifted and subjected to the same dilution as baryonic matter.

- *Dark matter (DM)* - The nature of the dark matter is unknown: it has been introduced to explain observations of galaxies' dynamics. It is the

26% of the matter of the universe and is probably formed by heavy, weakly-interacting particles. We expect that as the baryonic component:

$$\rho_D M(z) = \rho_{DM,0}(1+z)^3. \tag{2.20}$$

- *Dark energy (DE)* - The nature of this component is unknown: it has been introduced in order to explain the observed acceleration ($\ddot{a(t)} > 0$) in the expansion of the universe. Hence, eq. (2.14) requires a negative pressure. A suitable model for DE can be obtained introducing a *cosmological constant* (Λ) in eqs. (2.12) of general relativity. This leads to an equation of state with $w = -1$ and so:

  $$\rho_{DE}(z) = \rho_{DE,0} \tag{2.21}$$

  According to Planck Collaboration et al. 2015, dark energy accounts for the 69% of the energy of the universe.

As common in literature, let us define the parameters:

$$\Omega_{X,0} \equiv \frac{\rho_{X,0}}{\rho_c} \tag{2.22}$$

useful to describe the various components of the density as fractions of the critical density.

According to the cosmological standard model, the universe experienced two main epochs:

- at very high redshift ($z > 3300$) the main contribute to the total density comes from radiation: the universe experienced the *radiation dominated (RD) era.*

- For redshift $1 < z < 3300$ the universe is *matter dominated (MD)*: this is indeed the redshift range of interest in this work. Assuming the other components to be negligible, eq. (2.13) has as solution $a(t) \propto t^{2/3}$.

- At $z < 1$ the universe is dominated by the cosmological constant and the expansion is accelerated.

Having studied the evolution of the density of the various components of the universe, we can obtain from equation (2.13) the evolution of the Hubble parameter:

$$H(z) = H_0[\Omega_{m,0}(1+z)^3 + \Omega_{rad,0}(1+z)^4 + \Omega_{DE,0} + (1-\Omega)(1+z)^2]^{1/2}, \tag{2.23}$$

where $\Omega = \Omega_{m,0} + \Omega_{rad,0} + \Omega_{DE,0}$: the plot of eq. (2.23) is shown in figure 2.1.

The inverse of the Hubble parameter is the timescale of the expansion of the universe at redshift z, therefore it allows us to know what physical processes are relevant in a cosmological context: if the time scale of any process is higher than $H^{-1}(z)$ than it can be considered negligible.

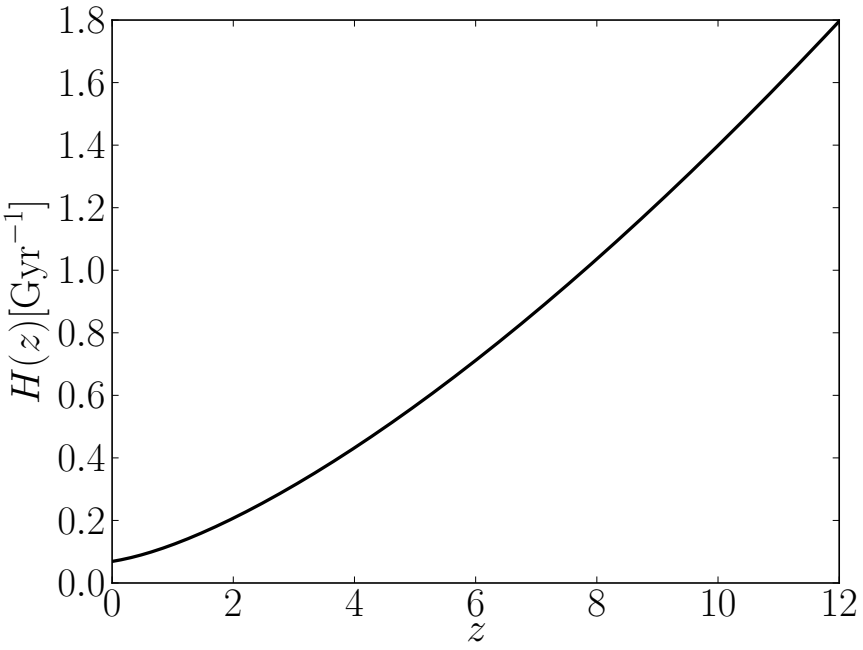

Figure 2.1: Hubble parameter as a function of redshift computed with the latest Planck data (Planck Collaboration et al. 2015)

From equation (2.7) and (2.23) we can obtain the time elapsed since the Big Bang at a given redshift z and the comoving distance that separate us from a source at redshift z:

$$\tau(z) = \int_z^\infty \frac{dz'}{(1+z')H(z')}, \tag{2.24}$$

$$x(z) = \int_0^z \frac{cdz'}{H(z')}. \tag{2.25}$$

Figure 2.2 show the plots of eqs. (2.24) , (2.25).

In this thesis, we will use the cosmological parameters:

- $H_0 = 67.7 \mathrm{km\,s^{-1}\,Mpc^{-1}}$,
- $\Omega_m = 0.3089$, with $\Omega_b = 0.049$,
- $\Omega = 1$,

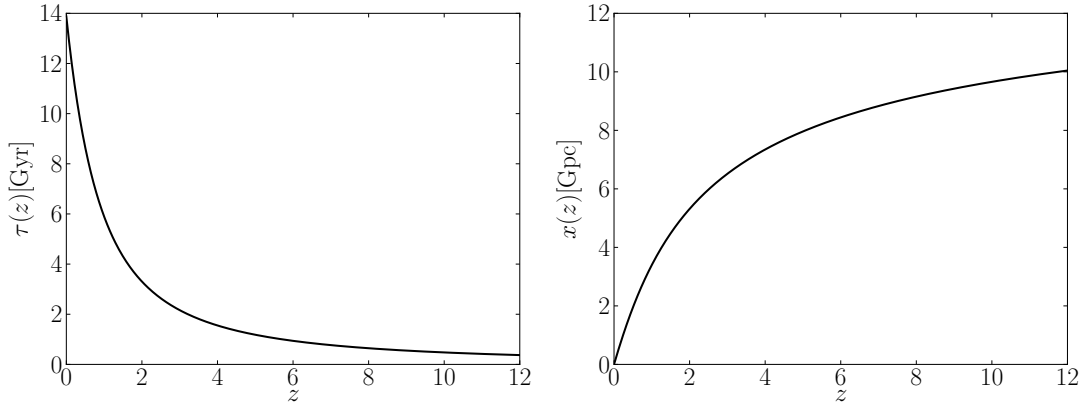

(a) Age of the universe **(b)** Comoving distance

Figure 2.2: Figure (a) shows the time elapsed since the Big Bang (eq. (2.24)). Figure (b) shows the redshift evolution of the comoving distance from us (eq. (2.25)).

from the last release of Planck collaboration data (Planck Collaboration et al. 2015). These values are consistent with a flat universe.

2.2 Structure Formation

In the previous section we considered the universe at the scales of homogeneity and isotropy, but it is sufficient to compare the typical densities on the Earth ($\approx 1\mathrm{g\,cm^{-3}}$) and in the intergalactic medium ($\approx 10^{-30}\mathrm{g\,cm^{-3}}$) to highlight that at small scales the universe is not homogeneous.

The detection of the Cosmic Microwave Background suggests that four-hundred-thousand years after the Big Bang our universe was almost homogeneous, with tiny density fluctuations ($\frac{\delta\rho}{\rho} \sim 10^{-5}$). Such fluctuations, due to gravitational instabilities, collapsed forming the large scale structures that we can observe in the local Universe.

The aim of this chapter is to introduce one of the most wide-spreading research field in cosmology: the formation of structures. To do so, we will first study the evolution of the first density perturbations in the linear regime (sec. 2.2.1), hence analyzing their growth in the simplest non-linear regime (sec. 2.2.2) and estimate the main features of a collapsed object (subsec. 2.2.3. To conclude this chapter, we will describe (in sec. 2.2.4) the statistical properties of the cosmic density field and introduce (sec. 2.2.5) a powerful theoretical tool to predict the density of collapsed halo as a function of mass at any given redshift.

2.2.1 Growth of linear perturbation

In this subsection we want to focus on the evolution of the tiny density fluctuations in the linear regime. In the high-redshift universe, we can neglect the cosmological constant that, as we will see in 2.2.5, suppresses the growth of perturbations.

The fluctuation field is described by a quantity called *overdensity* or *contrast*:

$$\delta(\mathbf{x},t) = \frac{\rho(\mathbf{x},t)}{\rho(t)} - 1 \ll 1. \tag{2.26}$$

Considering fluctuations with wavelength smaller than the Hubble radius $\lambda < c/H$ and with non-relativistic peculiar velocities, we can use the classical equation of fluid dynamics:

$$\begin{gathered}\left(\frac{\partial\rho}{\partial t}\right)_{\mathbf{r}} + \nabla_{\mathbf{r}}\cdot(\rho\mathbf{v}) = 0 \\ \left(\frac{\partial\mathbf{v}}{\partial t}\right)_{\mathbf{r}} + (\mathbf{v}\cdot\nabla_{\mathbf{r}})\mathbf{v} = -\frac{\nabla_{\mathbf{r}}P}{\rho} - \nabla\phi \\ \nabla^2_{\mathbf{r}}\phi = 4\pi G\rho.\end{gathered} \tag{2.27}$$

To disentangle the evolution due to the fluid dynamics to the one due to the expansion of the universe, we choose to work in comoving coordinates $\mathbf{x} = \mathbf{r}/a(t)$ and decompose the total velocity $\mathbf{v}$ in expansion velocity plus a peculiar velocity: $\mathbf{v} = \dot{a}\mathbf{x} + \mathbf{u}$.

In comoving coordinates:

$$\begin{gathered}\left(\frac{\partial f}{\partial t}\right)_{\mathbf{r}} = \frac{\partial f}{\partial t} - \frac{\dot{a}}{a}\mathbf{x}\cdot\nabla f \\ \nabla = a\nabla_{\mathbf{r}}.\end{gathered} \tag{2.28}$$

We also need to decompose the potential ϕ in unperturbed term and perturbation $\delta\phi$ and to use the equation of state $P(\rho)$ of the fluid:

$$\begin{gathered}\phi = \delta\phi + \frac{2}{3}\pi G\overline{\rho}a^2\mathbf{x}^2 \\ \nabla P = \frac{dP}{d\rho}\nabla\rho = c_s^2\overline{\rho}\nabla\delta\end{gathered} \tag{2.29}$$

where c_s is the speed of sound in the matter fluid.

From the previous equations, we obtain a second order differential equation for δ, known as the *Jeans equation*:

$$\frac{\partial^2\delta}{\partial t^2} + 2\frac{\dot{a}}{a}\frac{\partial\delta}{\partial t} = 4\pi G\bar{\rho}\delta + \frac{c_s^2}{a^2}\nabla^2\delta. \tag{2.30}$$

Eq. (2.30) tells us that the evolution of the perturbation is determined by two conflicting actions: gravity and the fluid pressure. The term $\propto \frac{\dot{a}}{a}$ is a drag term due to the expansion of the universe that slows down the growing of the perturbations.

If we want to study the physics in a matter dominated universe, we can neglect the pressure term; since $a(t) \propto t^{2/3}$, the Jeans equation simplifies in:

$$\frac{\partial^2\delta}{\partial t^2} + \frac{4}{3t}\frac{\partial\delta}{\partial t} = \frac{2}{3t^2}\delta, \tag{2.31}$$

which has only one non-vanishing independent solution:

$$\delta \propto t^{2/3} \propto a(t). \tag{2.32}$$

Hence, in an Einstein-de Sitter universe ($k, \Lambda = 0$), the perturbations grow proportionally to a growth factor $D(z) = 1/(1+z)$; in section 2.2.5 eq. (2.61) we will see that is in general more complicated. To solve Jeans equation (2.30), we will write it in Fourier Transform:

$$\frac{\partial^2\delta_{\mathbf{k}}}{\partial t^2} + 2\frac{\dot{a}}{a}\frac{\partial\delta_{\mathbf{k}}}{\partial t} = \left(4\pi G\overline{\rho} - \frac{k^2c_s^2}{a^2}\right)\delta_{\mathbf{k}}. \tag{2.33}$$

From right side of eq. (2.33) we can easily see that there is a characteristic scale k_J that distinguishes two different behaviours and has the dimension of the inverse of a length:

$$\lambda_J = \frac{2\pi a}{k_J} = \left(\frac{\pi c_s^2}{G\overline{\rho}}\right)^{1/2}. \tag{2.34}$$

The perturbation with a wavelength $\lambda < \lambda_J$ are oscillatory solution of eq. (2.33) and cannot collapse. Only the perturbation characterized by $\lambda > \lambda_J$ or mass:

$$M > M_J = \frac{4\pi}{3}\overline{\rho}\lambda_J^3 = \frac{4\pi}{3}\left(\frac{\pi c_s^2}{G\overline{\rho}^{1/3}}\right)^{3/2} \tag{2.35}$$

can collapse and form a non-linear object.

The quantities λ_J and M_J are known as *Jeans length* and *Jeans mass* respectively.

To consider also fluctuation on scales larger than the Hubble radius, we need

to include general relativity: we don't present a detailed analysis here, but show in table 2.1 the results from Padmanabhan 1993. It's worth to be noticed that, in the radiation dominated epoch, perturbations grow until they enter the Hubble radius: hence, we expect that in this phase small scale perturbations are suppressed with respect to the large scale one.

Epoch	radiation	DM	baryons
$t < t_{\rm enter} < t_{\rm eq}$	$\propto a^2$	$\propto a^2$	$\propto a^2$
$t_{\rm enter} < t < t_{\rm eq}$	osc	$\propto \ln a$	osc
$t_{\rm eq} < t < t_{\rm dec}$	osc	$\propto a$	osc
$t_{\rm dec} < t$	osc	$\propto a$	$\propto a$

Table 2.1: Evolution of linear fluctuations at different epochs. $t_{\rm enter}$ is the time at which a fluctuation enter the Hubble radius, $t_{\rm eq}$ is the time at which transition between a radiation and a matter dominated universe occurs, $t_{\rm dec}$ is the time of decoupling of radiation and baryons.

2.2.2 Spherical collapse

In the previous chapter, we have studied the growth of the perturbations in the linear regime. When the overdensity $\delta \simeq 1$, the linear analysis previously developed is no longer valid: the study of the non-linear collapse of an overdense region is very complex and requires a numerical approach in its general case. In this section we will study the special case in which the collapse occurs in spherical symmetry. We will neglect the contribution of the cosmological constant.

Let $M = \rho_b \frac{4\pi}{3} r_i^3 (1 + \bar{\delta}_i)$ be the total mass of the final collapsed object, where $\bar{\delta}_i = \frac{3}{4\pi r_i^3} \int_0^{r_i} 4\pi \delta_i(r) r^2 dr$ is the initial overdensity and ρ_b is the background density.

If $r_i \ll c/H$ we can neglect relativistic effects, describe the collapse with Newtonian gravity and write the energy per unit mass of a point particle at the proper coordinate r:

$$E = \frac{1}{2}\left(\frac{dr}{dt}\right)^2 - \frac{GM}{r}. \tag{2.36}$$

If $E \geq 0$ the system cannot stop its expansion and cannot collapse, while if $E < 0$ there is a specific $r = r_{ta}$ in which the kinetic term vanishes and the system will contract and collapse.

We want to evaluate E, so we evaluate the kinetic and the potential terms:

$$K_i = \frac{\dot{r}_i^2}{2} = \frac{H_i^2 r_i^2}{2} \tag{2.37}$$

$$U_i = \frac{GM}{r_i} = \frac{4\pi G}{3} \rho_b(t_i) r_i^2 (1 + \bar{\delta}_i) = K_i \Omega_i (1 + \bar{\delta}_i) \tag{2.38}$$

where $\Omega_i = \rho_b(t_i)/\rho_c(t_i)$. Then, the condition for collapse is the initial overdensity to be $\bar{\delta}_i > (\Omega_i^{-1} - 1)$.

Assuming to be in a flat, matter-dominated universe $\Omega_i = 1$, $H_i t_i \approx 2/3$ and $\delta_i \propto t_i^{2/3}$. Therefore, in a flat universe all the overdense regions will collapse. However, it is not true that at low redshift all the overdense regions are collapsed: the collapse time depends on the initial overdensity and diverges for $\overline{\delta}_i \to 0$; furthermore, we neglected the cosmological constant that becomes important at $z < 1$.

The equations of motion of the collapsing system have the parametric solutions:

$$r = A(1 - \cos\theta) \tag{2.39}$$

$$t = B(\theta - \sin\theta) \tag{2.40}$$

where A end B are:

$$A = \frac{3r_i}{10\bar{\delta}_i} \tag{2.41}$$

$$B = \frac{3t_i}{4(5\bar{\delta}_i/3)^{3/2}}. \tag{2.42}$$

At $t \approx t_i$ the overdense region expands with the Hubble flow, but according to the previous equations, the expansion gradually slows until the region reaches the radius of maximum expansion $r_{ta} = 2A$ at $t_{ta} = \pi B$.

Identify $\theta = 2\pi$ as the condition for collapse is a good approximation: even if it is a non-physical result (it assumes that different shells do not cross, and this is not valid in the late phases of collapse), more refined analysis show that at t_{coll} the structure is virialized (see next subsection) and hereafter we will use $t_{coll} = 2t_{ta}$ as collapse time.

For future purposes, it is useful to evaluate the density contrast that the linear theory predicts at the collapse time; since $\delta_l(t) = \delta_i a(t)/a(t_i) \approx \delta_i (t/t_i)^{2/3}$:

$$\delta_l(t_{ta}) = \delta_i \left(\frac{t_{t_a}}{t_i}\right)^{2/3} = 1.06 \tag{2.43}$$

$$\delta_l(t_{\rm coll}) = 2^{2/3}\delta_l(t_{\rm ta}) = 1.686 \tag{2.44}$$

We will see in section 2.2.5 that, for the Press-Schechter theory, this value represents a threshold: once the overdensity, obtained according to the linear theory, of a region reaches the amplitude $\delta_l(t_{\rm coll})$, it is considered a collapsed object.

2.2.3 Virialized dark matter halos

In the last section we discussed the theory of the spherical collapse. Although, in principle, a spherical region should collapse to a point mass, the existence of mechanisms of violent dynamical relaxation give life to a state of equilibrium known as *virialized dark matter halo*.

These halos are the basic structures from which all the complex objects that we observe in our universe form: in fact it is inside them that baryons collapse and give birth to the galaxies.

According to the *virial theorem*, in all dynamically relaxed, self-gravitating structures:

$$2K + U = 0 \tag{2.45}$$

where, for simplicity, we have neglected the cosmological constant term U_Λ. K and U are, respectively, the kinetic and potential energy of the baryonic matter (M_{gas}) contained in a virialized halo of mass M:

$$\begin{aligned} K &= \frac{3}{2}\frac{M_{gas}}{\mu m_p}k_B T \\ U &= -\frac{3}{5}\frac{GM_{gas}M}{r_{vir}}. \end{aligned} \tag{2.46}$$

Hence:

$$k_B T_{vir} = \frac{\mu m_p GGM}{5 r_{vir}}; \tag{2.47}$$

as a consequence of the virial theorem, the virial radius r_{vir} can be determined as one half of the turnaround radius, calculated in the previous section.

The final density contrast of the virialized structure is $\Delta_c(z) = \frac{\rho_{vir}(z)}{\bar{\rho}(z)}$ and it is approximately equal to 178 if the cosmological constant can be neglected.

From eq. (2.47), explicating the constants, we can obtain the temperature of a virialized halo of mass M at redshift z:

$$T_{vir}(M,z) \approx 19800K \left(\frac{\mu}{0.6}\right)\left(\frac{M}{10^8 h^{-1} M_\odot}\right)^{2/3}\left(\frac{\Omega_{m,0}\Delta_c(z)}{18\pi^2}\right)^{1/3}\left(\frac{1+z}{10}\right). \tag{2.48}$$

The value of the molecular weight μ of the gas strongly depends on the ionization fraction: in a fully ionized primordial gas $\mu \approx 0.6$, while in a fully neutral primordial gas $\mu \approx 1.2$.

2.2.4 Statistical properties of the density fluctuations

Hence we have not the possibility to reconstruct the actual realisation of the overdensity $\delta(\mathbf{x})$ at a given time in each point of the universe, the overdensity field is generally treated considering its properties as statistical ensemble.

This can seem a misplaced problem, because we know only one universe and it does not make sense to treat it with a statistical approach.

Anyway, we know from the cosmological principle that if we divide the universe regions of volume V sufficiently large, they all are perfectly equivalent, and it is sensible to ask what is the probability distribution function (PDF) to find at a given position $\mathbf{x}_i$ and at a given time a value of the overdensity field between δ_i and $\delta_i + d\delta_i$.

The statistical properties of the PDF (and so of the density field) are completely determined once one specifies its statistical moments. The simplest case is the one in which the PDF is a multivariate Gaussian, that has the great advantage to be completely specified by its second momentum: the two-points correlation function $\xi(r) =< \delta(x)\delta(x+r) >$. There are several arguments that support this approximation: for example it is predicted by inflationary models and it is in good agreement with experimental data from the CMB.

It is useful to work in the Fourier space, since the single modes evolve independently; the k-space PDF is still a Gaussian and its second momentum, the *power spectrum* is:

$$P(k) = \sigma_k^2 =< \delta_{\mathbf{k}}\delta_{\mathbf{k}}^* > . \tag{2.49}$$

$P(k)$ is strictly tied to the correlation function $\xi(r)$, being its Fourier transform.

A simple ansatz for the shape of $P(k)$ has been proposed by Harrison and Zel'dovich:

$$P_i(k) \propto k^n, \tag{2.50}$$

this shape is in good agreement with experimental data if $n = 0.97$ (Planck Collaboration et al. 2015). The normalization of the power spectrum is fixed from the galaxy surveys, as we will see in the next section.

We have already highlighted (reference) that, before the matter domination, perturbations grow as long as they enter the Hubble horizon, so different modes have different evolution; hence the power spectrum that seeded structure formation is different from the primordial one: the *processed* power spectrum is

$$P(k) \propto k^n T^2(k), \tag{2.51}$$

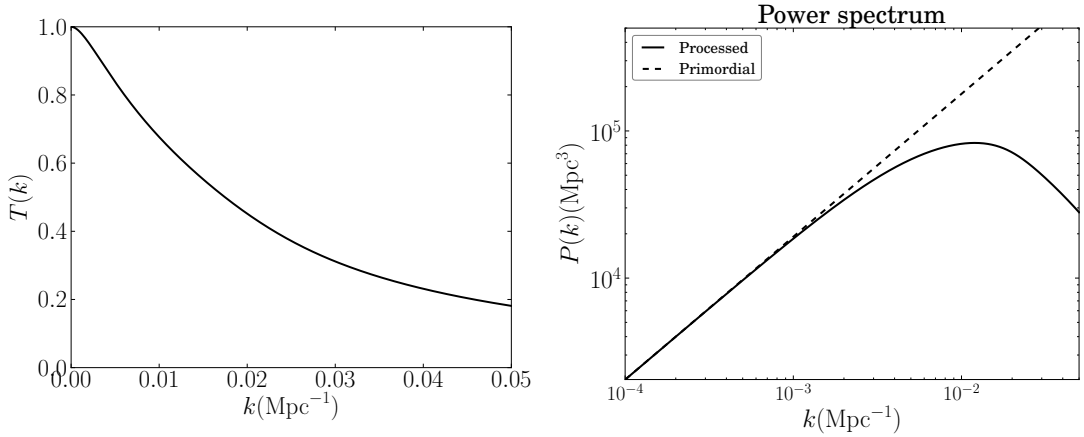

(a) Transfer function

(b) Power spectrum

Figure 2.3: Figure (a) shows the transfer function from Eisenstein and Hu 1998 . Figure (b) shows the primordial power spectrum (dotted line) and the processed one (solid line). The transfer function suppresses the scales above $k \approx 0.01$.

where the *transfer function* $T^2(k)$ suppresses the small scale fluctuations with λ smaller than the Hubble radius at the transition between the radiation dominated and the matter dominated era (that is $\approx$ 100Mpc). The transfer function by Eisenstein and Hu 1998 and the power spectrum are shown in fig. 2.3.

2.2.5 The halo mass function

One of the most useful prediction of the theory of structure formation is the number density of dark matter halos as a function of mass at any given redshift z. Press and Schechter (PS) in 1974 derived a simple analytic model to build a distribution function for collapsed object: once a region on the fixed mass scale of interest reaches the threshold amplitude for collapse (eq. (2.44)) obtained according to the linear theory, it can be declared a virialized object.

In order to assign masses to this collapsed regions Press and Schechter considered a smoothed density field on a scale R:

$$\delta_R(\mathbf{x}) = \int \delta(\mathbf{x}+\mathbf{x}')W(R,\mathbf{x})d^3\mathbf{x}', \tag{2.52}$$

where W is a suitable *window function*. The W used in the formal derivation of the mass function is

$$W(R,\mathbf{x}) = 4\pi R^3 \frac{\sin kR - kR\cos kR}{(kR)^3}, \tag{2.53}$$

a top-hat in the $\mathbf{k}-$space that cuts out sharply all the details on scales smaller

than R. $V_W = \int d^3\mathbf{x} W(\mathbf{x}) = \frac{4\pi}{3}$ is the equivalent of the volume of this window.

The excess of mass contained around a point $\mathbf{x}$ is

$$\delta M(x) = \int d^3\mathbf{y}\delta\rho(\mathbf{y})W(\mathbf{x}-\mathbf{y}) = \int \frac{d^3\mathbf{k}}{(2\pi)^3}\tilde{\delta}_{\mathbf{k}}\bar{\rho}\tilde{W}(\mathbf{k})e^{i\mathbf{k}\cdot\mathbf{x}} \tag{2.54}$$

For the central limit theorem, $\delta M/M$ has a Gaussian distribution and a standard deviation that can be written in terms of the power spectrum:

$$\sigma_M^2(R) = \langle|\delta M/M|^2\rangle = \frac{1}{2\pi^2 V_W^2}\int_0^\infty k^2 dk \sigma_k^2 \tilde{W}_k^2. \tag{2.55}$$

The normalization of the power spectrum can be fixed from the observational value of σ_M on the scale of $R = 8h^{-1}$Mpc, $\sigma_8 = 0.82$ (Planck Collaboration et al. 2015).

According to Press and Schechter 1974, the fraction of mass elements contained in collapsed objects with mass greater than M at redshift z is the same as the probability that the present day linear extrapolated density yield at $\mathbf{x}$, δ_M, is greater than $\delta_c = 1.686$:

$$F(>M,z) = \frac{1}{2}\mathrm{erfc}(\nu_c) \tag{2.56}$$

where $\nu_c = \delta_c/\sigma(M,z)$. This distribution is not correctly normalized: in fact, one sees that $F(>0,z) = 1/2$ while it is reasonable to be 1.

This problem arise from the *cloud-into-cloud problem*: eq. (2.56) ignores all the regions that have $\delta_{M_1} < \delta_c$ when smoothed on a scale M_1 but have $\delta_{M_2} > \delta_c$ when smoothed on a larger scale $M_2 > M_1$ (that is all that regions that are not part of a collapsed object strictly greater than M_1 but are part of a collapsed object greater than M_2).

Press and Schechter 1974 corrected the problem simply multiplying $F(>M,z)$ for a factor 2.

Finally, the PS mass function is:

$$\frac{dn(M,z)}{dM} = -\frac{\bar{\rho}}{M}\frac{\partial F(M,z)}{\partial M} = \frac{\bar{\rho}}{M^2}f_{PS}\left|\frac{d\ln\nu}{d\ln M}\right| \tag{2.57}$$

with

$$f_{PS}(\nu_c) = \sqrt{\frac{2}{\pi}}\nu_c \exp\left(-\frac{\nu_c^2}{2}\right) \tag{2.58}$$

The presence of the factor 2 in the previous equations, can be obtained with a more corrected, self-consistent approach (the excursion set formalism). This method allows us to compute also conditional mass distributions, such as the one

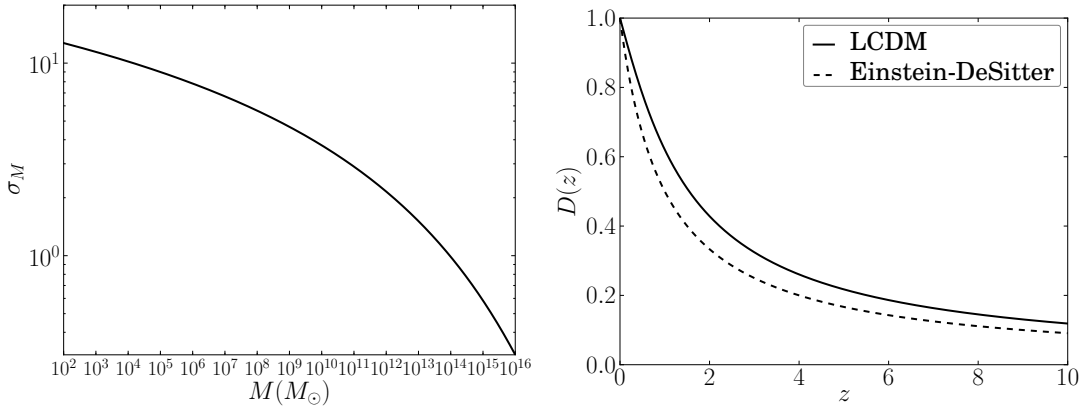

(a) Standard deviation **(b)** Growth factor

Figure 2.4: Figure (a) shows the standard deviation $\sigma_M(z=0)$. Figure (b) shows the growth factor in an Einstein-de Sitter universe (dashed line) and the one from Carroll et al. 1992 (solid line): as can be seen, the presence of a cosmological constant slows the growth of the perturbations.

of the *progenitors* of a certain dark matter halo. Consider a collapsed object of mass M_1 at redshift z_1 so that it has a linearly extrapolated density contrast $\delta_1 = \delta_c(z_1)$; then, the mass distribution of its progenitors at $z_2 > z_1$ is:

$$n(M_2, z_2|M_1, z_1)dM_2 = \frac{M_1}{M_2^2}\left|\frac{d\ln\nu_{12}}{d\ln M_2}\right| dM_2 \tag{2.59}$$

where:

$$\nu_{12} = \frac{\delta_2 - \delta_1}{\sqrt{\sigma^2(M_2) - \sigma^2(M_1)}} \tag{2.60}$$

The PS formalism provides a simple way to understand why the structure formation is *bottom − up* (i.e. hierarchical). As is shown in fig. 2.4a, σ_M is a decreasing function of mass, because $\sigma_M^2 \sim k^{3+n} \sim R^{-(n+3)} \sim M^{-\frac{n+3}{3}}$. In section 2.2.1 we saw that in a matter dominated epoch the perturbation grows with the scale factor $\delta \propto D(z) = 1/(1+z)$. In presence of the cosmological constant, the growth of the fluctuation is inhibited and the expression of the growth factor $D(z)$ is a more complicated. In this thesis, we refer to the fitting formula of Carroll et al. 1992:

$$D(z) = \frac{g(z)}{g(0)(1+z)} \tag{2.61}$$

where

$$g(z) = \frac{5}{2}\omega_m(z)\left[\omega_m(z)^{4/7} - \Omega_{DE}(z) + \frac{1+\omega_m(z)/2}{1+\Omega_{DE}(z)/70}\right]^{-1}. \tag{2.62}$$

The previous formula is plotted in fig. 2.4b, where a comparison with the growth

factor in an Einstein-de Sitter universe is shown.

Then:

$$\sigma_M(M,z) = D(z)\left(\frac{M}{M^*}\right)^{-(n+3)/3} = \left(\frac{M}{M_{NL}(z)}\right)^{-(n+3)/3} \tag{2.63}$$

The mass scale at which fluctuations become non linear, $M_{NL} = \frac{M^*}{D(z)^{(n+3)/3}}$ (according to Eisenstein and Hu 1998 is always $n > -2$) is a decreasing function of redshift: smaller scales become enter this regime before larger ones.

Hence, the structures formation is *bottom-up*: smaller halos, that form first, merge to form more massive halos. In the next chapters, we will see that this statement leads to a very important hypothesis: the possibility that black holes could also accrete through merging of smaller ones.

3 Active Galactic Nuclei

In this chapter, we introduce one of the brightest type of objects in the universe, the active galactic nuclei (AGNs), and we will discuss the physical mechanisms that drive their emission.

In the first section we will do a brief introduction to active galaxies and report their main observational features. Since the most accredited model assume that the AGNs' central engine is powered by an accreting supermassive black hole (SMBH), in section (3.2) we will give a general description of a BH as solution of Einstein equations. Then, in section 3.3, we will focus on the accretion mechanisms, describing the main characteristics of a spherical accretion (subsec.3.3.1) and the high radiative efficiency of an accretion disk (subsec.3.3.2).

3.1 Active Galaxies

The names *active galaxies* and *active galactic nuclei* (AGNs) refer to the main feature that distinguishes these objects from ordinary (i.e. inactive) galaxies: the presence of an accreting supermassive black hole (SMBH) in their center.

At the present time, more than one million of this kind of sources had been detected and it has been estimated (Netzer 2013) that in the local universe (i.e. $z \leq 0.1$) about 1 out of 50 galaxies contains a fast accreting SMBH and about 1 out of 3 contains a slowly accreting SMBH.

Although all objects powered by an active SMBH are now known as AGNs, they have several different names, relics from the 1960s - 1970s, originating from an early confusion among sources with different observational signatures. These objects are now unified in a standard model; among them:

- *Seyfert galaxies*- these galaxies present a high surface brightness and a bright nucleus. Their emission is characterized by strong ionization lines. This category distinguishes in *Type I* and *Type II* Seyfert galaxies: the first type show strong, very broad emission lines that are not found in the second type.

- *Quasars* (QSOs) present very strong broad emission lines but, unlike Seyfert galaxies, their host galaxy is usually not clearly detected. As a common habit, astronomers usually call "quasars" high-redshift AGNs in general, hence, since this work is focused on high-z quasars, we will use "QSO" or "AGN" equivalently.

- *Blazars* are the only kind of AGN that present a γ-ray emission. These objects are extremely rare because, as we will explain, the detection of γ-ray emission occurs only when there are relativistic outflows from the nucleus, oriented along our line of sight.

- *LINERs* (low-ionization nuclear emission-line region) are characterized from an emission of low-ionized or neutral atom lines and contain a weakly active nucleus.

The objects reported in the previous list contain also other subcategories, that for brevity will not be presented in this work.

The *unified AGNs model* interprets the observational differences among these sources as arising from different viewing angles to the center of the sources and from the eventual presence of a large amount of obscuring material along the line of sight. Astronomers gather AGNs in two large groups:

- *type-I AGNs*, that are not obscured along our lines of sight to their center;

- *type-II AGNs*, with heavy obscuration along the line of sight, that extincts almost all the optical-UV radiation from the inner parsec.

Figure 3.1 shows a highly simplified scheme of AGN unification, whose main features are:

- a SMBH surrounded by a thin *accretion disk* that represents the central engine that power an AGN. See sec.3.3.2.

- a *dusty torus*: a thick structure of obscuring material that surrounds the accretion disk at distance of order 1 pc and covers a significant portion of solid angle. The torus causes the dimming that characterizes type II AGNs.

- a *broad line region* (BLR) totally enclosed in the torus, that contains line emitting clouds. The lines are broadened by Doppler effect, due to the high Keplerian velocity of the clouds around the black hole.

- a *narrow line region* (NLR) which extends from a few to several thousand parsecs; being settled farther from the nucleus, the emitting clouds that produce narrower lines.
- the *relativistic jets*: twin collimated, fast outflows in opposite directions, whose detection occurs only along our line of sight. They are present only in the 10% of the AGNs and are often accompanied by a radio emission.
- the *host galaxy* that it is often unresolved with respect to the nucleus. Anyway, even if the host galaxy does not contribute much to the luminosity of these sources, its interstellar medium (ISM) play an important role in the attenuation, as we will see in section 5.3.

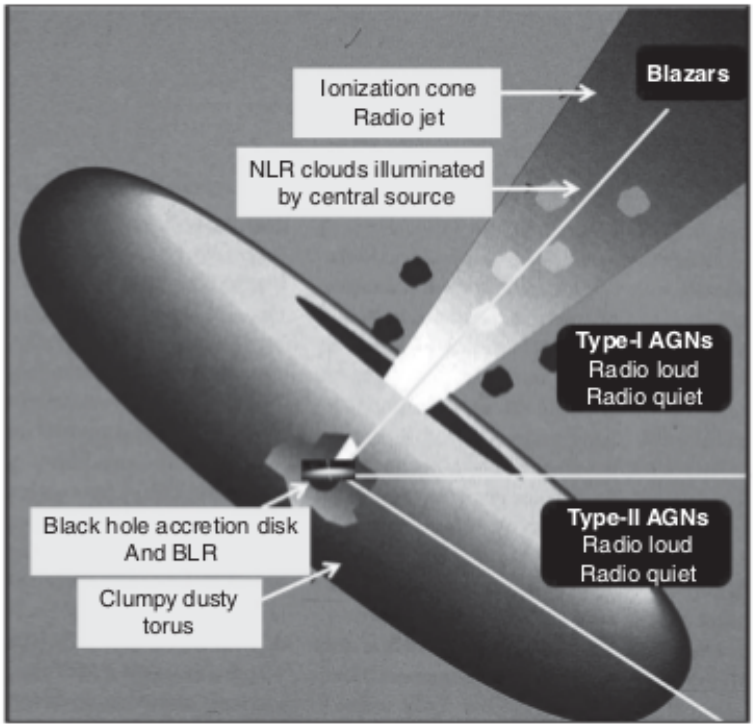

Figure 3.1: A side view of AGNs showing the main concepts of the unification scheme, by Netzer 2013 .

Studying the spectral characteristics of AGNs, astronomers usually analyze the spectral energy distribution (SED), described in terms of monochromatic luminosity per unit frequency ($L_\nu[\mathrm{erg\,s^{-1}\,Hz^{-1}}]$), wavelength ($L_\lambda[\mathrm{erg\,s^{-1}\,cm^{-1}}]$) or energy ($L_E[\mathrm{erg\,s^{-1}\,erg^{-1}}]$).

Unlike stellar sources AGNs present a significant emission in the whole electromagnetic spectrum, hence we conclude AGNs' description with a brief review of the main observational features of an AGN in the various emission band:

- *Radio*: many AGNs presents single or double-lobes structures (that can exceed in extension the host galaxies) and strong radio cores and/or radio jets from the nucleus. If an AGN shows a radio emission with monochromatic luminosity at 5 GHz at least ten times stronger than the monochromatic luminosity in the B optical band, it is called *radio-loud*, otherwise *radio-quiet*. Statistics on large numbers shows that $\sim 10\%$ of AGNs are radio-loud sources: this provides a way to identify AGNs in deep radio surveys; stars are extremely weak radio emitters, so an optical pointlike source that is also a strong radio source is likely to be a radio-loud AGN. The positional resolution of radio surveys is of order of 1 arcsec and usually there are no problems in confirming that the radio source and the optical one are the same source: most of the early AGNs samples were discovered in this way.

- *IR*: most of the emission in the near infra-red (NIR) and the mid-infra-red (MIR) is due to secondary (i.e. that is not the direct result of the accretion process itself) thermal emission from the dusty structure (the torus) within 1 pc around the central source. The temperature of the NIR and MIR emitting dust is between 100 and 200 K. Most of the far infra-red (FIR) thermal emission is thought to be due to colder dust heated by young stars present in the host galaxy.

  Observations in the IR band allow us to detect highly obscured AGNs: a large fraction of such an objects would not been recognized as AGNs according to their non-detectable optical and X-ray emission, but their MIR spectrum is dominated by warm dust emission. Hence, the observation in this band provides a complementary technique to detect AGNs.

- *Optical and UV*: optical images of type-I AGNs show evidence of a pointlike central sources with an emission that can dominate over the stellar background of the hosting galaxy: the non-stellar origin of this emission excess is determined by the SED shape and the absence of strong stellar absorption lines. In the local universe, many AGNs are much fainter than their host and the contamination by stellar light must be taken into account in optical observations.

- *X-rays*: relative AGN luminosity increases with decreasing wavelengths and the contamination by stars is no more a major problem; unlike stellar sources, almost all AGNs are strong X-ray emitters. AGNs' X-ray emission play a very important role in this work: in chapters 5 and 6 we will study the visibility of the faint progenitors of luminous quasars in this band.

A single power-law $L_\nu \propto \nu^{-\alpha_X}$ fits well the intrinsic (i.e. unobscured) spectrum of many types of AGNs over the energy range 0.2-20 keV. Observatively, $\alpha_X \sim 1$ (Piconcelli et al. 2005). The most sensitive X-ray surveys had been able to detected very distant ($z \sim 7$ or even more) sources with strong 0.5-2 keV (in the observatory rest frame) emission; type-II AGNs with obscuring column densities ($N_{HI} > 10^{22}\text{cm}^{-2}$ or more) are more difficult to be detected. The deepest surveys ever performed at the present times are the ones by the Chandra Space Telescope, that has a resolution of ~ 1 arcsec. The Chandra X-ray Observatory is characterized by a passband that is extended up to about 20 keV. However, these missions cover only a small area of the sky: at the end of this thesis, in chapter 6, we will discuss the potentiality of these powerful observatories in the search for the faint SMBHs' progenitors as X-ray emitters.

- $\gamma-$*rays*: to conclude the description of AGNs' emissivity, it is worth to mention that observations above 100 keV show that the majority of AGNs are weak high-energy emitters. On the other hand, less than the 10% of them present a strong $\gamma-$ray emission: unfortunately, the current $\gamma-$ray observatories (such as the Fermi Gamma-Ray Space Telescope) have low spatial resolution and all AGNs revealed at these energies appears as point sources, but they allow us to probe their high-energy emission up to 300 GeV.

Having described what active galactic nuclei are, in the following section we will introduce their central engines: the black holes.

3.2 Black Holes

Since the scientific community agrees that the central engine of an AGN is an accreting supermassive black hole (SMBH), in this section we will present a short description of black holes (BH) in the context of the general relativity. Black holes (as well as pulsars and neutron stars) had been considered a mere theoretical curiosity for a long time. The idea of a body so massive that even light itself could not escape is ascribed to John Michell and Pierre-Simone Laplace in the XVIII century; in particular, the first publication related to such an object is a letter by Michell to Henry Cavendish in 1783 to the Royal Society:

If the semi-diameter of a sphere of the same density as the Sun were to exceed that of the Sun in the proportion of 500 to 1, a body falling from an infinite height

towards it would have acquired at its surface greater velocity than that of light, and consequently supposing light to be attracted by the same force in proportion to its vis inertiae, with other bodies, all light emitted from such a body would be made to return towards it by its own proper gravity.

Such idea of "dark stars", promoted in 1796 by Laplace in his book *Exposition su systéme du Mond*, had nothing to do with the idea of space and time, which where considered absolute concepts: a dark star was conceivable only between the framework of the Newtonian theory of matter and gravitation and the object beyond the horizon was rigid, stable against collapse.

It was only in the XIX century, with the development of the theory of General Relativity, that BHs were studied in the general space-time framework as particular solution of Einstein's field equations.

3.2.1 Black Holes as solution of Einstein equations

Developed by Albert Einstein between 1907 and 1915, with contribution of many others after 1915, the theory of General Relativity totally revolutionized the concepts of space and time.

As can be done with every physical property, space and time can be represented with a mathematical structure: in relativity an event that happened in a given space point at a given time is represented as an element of a 4-D real manifold x^μ (where x^0 corresponds to the time coordinate and x^i, with $i = 1, 2, 3$, to the spatial coordinates). Then, if we want to calculate a distance between two events, we need to introduce a geometrical structure on this manifold; this can be done defining a metric tensor (briefly, a *metric*) that allows us to calculate distances. In the Euclidean space, for instance, the metric tensor is a Kronecker delta function, while in the Minkowskian space it is:

$$\delta_{\mu\nu} = \begin{pmatrix} 1 & 0 & 0 & 0 \\ 0 & -1 & 0 & 0 \\ 0 & 0 & -1 & 0 \\ 0 & 0 & 0 & -1 \end{pmatrix} \tag{3.1}$$

and the distance ds between two arbitrarily close events is:

$$ds^2 = \delta_{\mu\nu} dx^\mu dx^\nu. \tag{3.2}$$

Since, in general relativity, gravity is the result of the curvature of the space-time, a key issue of the theory is to determine the geometry of the space-time

(and so the effects of gravity) finding a law that establishes a relation between gravitational sources and the metric: this law is expressed in the Einstein equations (see chapter 2, eqs.(2.12)). The derivation of the Einstein equations and the discussion of its solutions lies outside of the aims of our thesis and involve several quantities and mathematical tools that we will not introduce in this work. Hence, we will focus on those solutions of Einstein equations that directly concern our study field, beginning from the one found, in 1916, by Karl Schwarzschild: it describes the geometry of the space-time in the vacuum region outside a static, spherical object of mass M, with the whole mass assumed to be concentrated at $r = 0$. The Schwarzshild metric expressed in spherical coordinates (t, r, θ, ϕ) is:

$$ds^2 = (1 - \frac{2GM}{rc^2})c^2dt^2 - (1 - \frac{2GM}{rc^2})^{-1}dr^2 - r^2(d\theta^2 + \sin^2\theta d\phi^2). \tag{3.3}$$

There are two singularities in the metric: $r = 0$ and $r_{Schw} = \frac{2GM}{c^2}$; the first one is a physical singularity and it is uneradicable, the second one, instead, is a singularity of the metric (3.3) and can be eliminated with a change in the coordinates.

The quantity r_{Schw} is known as *Schwarzschild radius* r_{Schw} and corresponds to the surface that represents the *horizon of events*: no signal can reach us from the inside (for details, refer to Schutz 1985 and Romero and Vila 2013). Although a Schwarzschild radius can be associated at every object of mass M, at ordinary densities it lies well inside the object: for instance, for the Sun $r_{Schw} \approx 3\,\text{km}$ and for the Earth r_{Schw} is less than a centimeter.

Several solutions of the Einstein equations (in primis, the Kerr solution that describes a rotating BH) should be introduced in order to fully understand the phenomenology related to a BH, but such a description lies well outside of the aims of this work. We limit ourselves to provide some references, (Schutz 1985) and (Romero and Vila 2013), and to explore, in the next section, one important physical process that allows us the detection of such mysterious objects: their accretion.

3.3 BH accretion

A BH is a rather simple physical object (for the "no-hair theorem" it can be completely described by its mass, electric charge[1] and angular momentum [2]) nevertheless, it has a great impact on its surrounding environment.

Accretion on a black hole, in particular, is one of the main radiation source in high energy astrophysics: in the accretion process, for the energy conservation law, the decreasing of the potential energy is compensated by an increasing kinetic energy. If part of this kinetic energy is converted in thermal energy, a large quantity of radiation is emitted.

The most important feature of an accretion process is its high efficiency: Thorne 1974 had shown through theoretical argumentations that the radiative efficiency ranges from $\eta = 0.057$ for a Schwarzschild (i.e. non-rotating) black hole to $\eta = 0.32$ for a maximally rotating object; on the other hand, if we consider for comparison the energy that could be extracted from the mass by nuclear fusion reaction, the matter-radiation conversion factor is computed to be lower than 0.01.

One of the most important concept about energy sources is that the luminosity produced by the source itself (or, in our case of interest, in its surrounding environment) affects its external layers. In an accretion process, it means that the emitted radiation can block the infall.

Let us consider an accretion process in spherical symmetry, with metal-free, completely ionized, accreting material. If the photons emitted by the source have energy < 100keV, the main interaction between the photons and the gas is the Thomson scattering.

If a source have luminosity L, the momentum carried by the photons for unit time is L/c and the momentum for unit time and unit surface (at distance r from the source) is $L/4\pi r^2 c$. Being the Thomson scattering an isotropic process, on average an electron takes all the momentum of the incident photon. Not every electron interacts: the probability of interaction is expressed through the Thomson cross section σ_T.

Hence, if there are n_e electrons for unit volume, the force perceived by the gas is:

$$F_r = \frac{L}{4\pi r^2 c}\sigma_T n_e \tag{3.4}$$

[1] However, electric charge can be safely ignored because macroscopic objects are very nearly neutral.

[2] The Schwarzschild BH described in the previous section is not rotating; however, general relativity predicts the existence of rotating BHs, well described by the Kerr metric (1963).

In the accreting material, electrons and protons are strongly coupled by the electrostatic force that prevent them to separate, hence this force (that has effect mostly on electrons because $\sigma_T \propto m^{-2}$ and $m_p \gg m_e$) have to be compared with the gravitational force on protons.

$$F_g = n_e \frac{GMm_p}{r^2} \tag{3.5}$$

At equilibrium, $F_g = F_r$ and the luminosity assumes a value known as *Eddington luminosity*:

$$L_E \equiv \frac{4\pi cGMm_p}{\sigma_T} \approx 1.5 \times 10^{38} \frac{M}{M_\odot} \mathrm{erg} \cdot \mathrm{s}^{-1}. \tag{3.6}$$

The Eddington luminosity represents an upper limit for the luminosity of stationary (i.e. not explosive) sources: for $L \gg L_E$ (as occurs in a supernova) the radiation pressure would block the accretion flux, that fuels the emission itself.

In the first part of this section, we have talked about the radiative efficiency: the matter-radiation conversion factor η at which radiation is generated by a matter flux $\dot{M}$ is defined as:

$$L \equiv \eta \dot{M} c^2. \tag{3.7}$$

Assuming $\eta = 0.1$ as usual in literature (Vietri 2006, Petri et al. 2012, Volonteri and Stark 2011 and Frank et al. 2002), we can estimate the *Eddington accretion rate* accreted on a compact object in order to produce an Eddington luminosity:

$$\dot{M}_E \equiv \frac{L_E}{\eta c^2} = 2.5 \times 10^{-8} \frac{M}{M_\odot} \frac{0.1}{\eta} M_\odot \mathrm{yr}^{-1}. \tag{3.8}$$

Has already highlighted, according to Thorne 1974 the radiative efficiency ranges from $\eta = 0.057$ for a Schwarzschild (i.e. non-rotating) black hole to $\eta = 0.32$ for a maximally rotating object.

Assuming that the fraction of mass that is not converted in radiation is actually accreted by the compact object (that in our case of interest is a BH), the growth rate of the black hole is: $\dot{M}_{BH} = \dot{M}(1 - \eta)$ and its bolometric luminosity (3.7) can be written as:

$$L = \dot{M}_{BH} \frac{\eta c^2}{1 - \eta}. \tag{3.9}$$

The time scale for the growth of a BH that is accreting at the Eddington rate is: $\tau_E = \frac{M_{BH}}{\dot{M}_{BH}} = t_E \frac{\eta}{1-\eta}$, where the quantity t_E is called *Eddington time*.

3.3.1 Bondi accretion

Let us consider the accretion on a BH in the most simple case: we will assume that the system is endowed with spherical symmetry, that the accreting gas is well described from a polytropic relation $PV^\gamma = constant$ and that the situation is stationary (so that $\partial/\partial t = 0$).

Under these hypothesis, the mass conservation law can be written as:

$$0 = \frac{\partial \rho}{\partial t} + \nabla \cdot (\rho \vec{v}) = \frac{1}{r^2}\frac{\partial}{\partial r}(r^2 \rho v_r) = 0 \tag{3.10}$$

that, integrated, give us the mass accreted per unit time:

$$\dot{M} = 4\pi \rho v_r r^2. \tag{3.11}$$

Let us fix the boundary condition of the problem, in order to determine $\dot{M}$: the accretion starts at large distance from the center, where the gas is at rest and density and pressure are ρ_∞ and P_∞.

For the Bernoulli theorem, we know that the quantity $\frac{v_r^2}{2} + w + \phi$ is conserved, hence:

$$\frac{v_r^2}{2} + w - \frac{GM}{r} = w_\infty, \tag{3.12}$$

where $w = \epsilon + P/\rho = \gamma P/((\gamma - 1)\rho)$ is the specific enthalpy (being ϵ the internal energy of the system for unit mass).

If we change coordinates, taking the sound speed at infinity $c_{s_\infty}^2 = \gamma \frac{P_\infty}{\rho_\infty}$ as unit of velocity, ρ_∞ as a unit density and the accretion radius (at which the sound speed equals the free fall speed) $r_a = \frac{2GM}{v_s^2}$ as a unit of distance (so that $r = r_a \xi$, $\rho = \rho_\infty R(\xi)$), then $\dot{M}$ is completely specified by a parameter λ so that:

$$\dot{M} = 4\pi \lambda \frac{G^2 M^2 \rho_\infty}{c_{s_\infty}^3}. \tag{3.13}$$

Resolving the differential equations (3.13) and (3.12), we find that there is only one value of the parameter λ that respects the condition of continuity at the sonic point (i.e. the point in which $v_r = c_s$):

$$\lambda = \left(\frac{1}{2}\right)^{\frac{\gamma+1}{2(\gamma-1)}} \left(\frac{5-3\gamma}{4}\right)^{-\frac{5\gamma-3}{2(\gamma-1)}} \tag{3.14}$$

With this value of λ, the accretion rate in equation (3.13) is called *Bondi accretion rate* and depends on the mass M, on the initial conditions and on the equation of state, since λ depends on γ.

Shapiro 1973 had shown that the radiative efficiency of the Bondi accretion on a BH is very low: $\eta_{Bondi} \approx 10^{-4}$. This occurs because there is not a non-thermal electrons population because, since the black hole have not a solid surface, there cannot be shock waves that accelerate them. Hence, the only possible radiative process is the *bremsstrahlung*: if the gas density is low, the cooling time is longer than the free fall time, otherwise if the gas is dense, the time scale of the diffusion of the photons outward is longer than the free fall time. In any case, the main part of the released potential energy is not converted in thermal energy and cannot be radiated away.

3.3.2 Accretion disks

In the previous section we analyzed the spherical accretion on a compact object. Anyway, in the majority of the astrophysical situations, the accreting matter is endowed with an amount of angular momentum that does not allow it to fall in merely radial direction on a BH.

General relativity predicts the existence of an innermost stable orbit, that corresponds to a minimum angular momentum of order $j_{min} = qGM/c$ (Vietri 2006), where the adimensional parameter q is order of unity. Thus, all the accreting elements that possess an angular moment $j > j_{min}$ will arrange themselves in a disk perpendicular to the rotational axis. To make an example, let us consider a BH of mass $\approx 10^8 M_\odot$ and assume that the accreting material comes from the whole galaxy (so it rotates with velocity of order 100 km/s at distances of order 1 kpc): then $j \approx 3 \times 10^{28} \mathrm{cm}^2\mathrm{s}^{-1}$ and $j_{min} \approx 4 \times 10^{23} \mathrm{cm}^2\mathrm{s}^{-1} << j$.

In this subsection, we want to investigate the structure and the emissivity of a Keplerian, thin disk: in fact, being the spherical accretion process not radiatively efficient, it is thought that accretion disks provide most of AGNs' emission. In a Keplerian system the only force that is acting on the gas is the gravitational one, that is a *central* force, i. e. it preserves the angular momentum. Hence, the disk accretion requires a physical mechanism that forces a rearrangement of the angular momentum of the fluid.

As a classical analogue, two rings of matter in centrifugal equilibrium have angular velocity $\omega_K = GM/r^3$: the two rings slide one against the other, one rotating faster than the other. There are friction forces, identical in modulus and opposite, acting on the two rings: hence, the total angular moment of the system does not change; the amount of angular momentum lost by the inner ring is gained by the outer one. From this simple classical argumentation it is clear that in an accretion disk the angular momentum tend to shift outward.

Let $G(r)$ be the total torque that the material external to the radius r apply on the fluid within the radius r. Two condition have to be satisfied for the accretion process to happen. First of all, in order to fall on the BH the material has to loose angular momentum, hence:

$$G(r) < 0. \tag{3.15}$$

Then, considering a ring of material centered in r of infinitesimal thickness dr, it applies a torque on the inner ring and undergoes a torque from the outer ring. The total torque for unit thickness that acts on the ring is $\partial G(r)/\partial r$; then, in order of the ring to undergo a loss of angular moment, it has to be:

$$\frac{\partial G(r)}{\partial r} < 0. \tag{3.16}$$

If these two relations are satisfied, in the disk there is a outward flux of angular momentum.

So far, we have not specified the nature of the torque. We save this topic for the final part of this section, highlighting for the moment some important results that can be obtained in a totally general way without specifying $G(r)$.

Assume that the disk is infinitely thin: then it is characterized by a surface density Σ. The continuity equation is, in cylindrical coordinates and reminding the axial symmetry of the disk:

$$\frac{\partial \Sigma}{\partial t} + \frac{1}{r}\frac{\partial}{\partial r}(r v_r \Sigma) = 0. \tag{3.17}$$

The angular momentum is not a absolutely conserved quantity, as can be the mass or the electric charge: it can change if the mass in the considered volume is undergoes a torque. Hence, the equation that gives us the conservation of the angular momentum L along the rotational axis $\vec{z}$ is:

$$\frac{\partial L_z}{\partial t} + \frac{1}{r}\frac{\partial}{\partial r}(r v_r L_z) = \frac{1}{2\pi r}\frac{\partial G}{\partial r} \tag{3.18}$$

In the stationary case, the last two equations can be easily integrated to get:

$$\dot{M} = -2\pi r v_r \Sigma \tag{3.19}$$

$$F_L = -r^2 \omega \dot{M} - G(r) \tag{3.20}$$

where $\dot{M}$ is the accretion rate on the BH and F_L is the flux of angular momentum, that consists of a negative term due to the matter transport (advection term: the matter that accretes on the compact object retains some of its angular momentum) and a positive term (remember eq. (3.15)) due to the torques between the disk's elements (it removes angular momentum and transports it outward).

If the material that falls above the last stable orbit r_m retains all its angular momentum, $F_L = \dot{M}(GMr)^{1/2}$, otherwise, if it retains only a fraction β of its angular momentum:

$$F_L = \beta\dot{M}(GMr)^{1/2} \tag{3.21}$$

So that, eq. (3.20), can be rewritten:

$$r^2\omega\dot{M}R(r) = -G(r) \tag{3.22}$$

where $R(r) \equiv 1 - \beta\frac{r_m^2\omega_m}{r^2\omega}$, where ω_m is the Keplerian velocity at r_m, so that at $r \gg r_m$ the two terms are almost perfectly balanced.

Consider again the two rings that apply a mutual torque N. The equation of motion for the two rings will be: $\frac{dJ_1}{dt} = -N$, $\frac{dJ_2}{dt} = N$. If we assume the moment of inertia to be constant, the change of kinetic energy is:

$$\frac{d}{dt}\left(\frac{\omega_1 J_1 + \omega_2 J_2}{2}\right) = -N(\omega_1 - \omega_2) \approx dr\frac{dN}{dr}N < 0 \tag{3.23}$$

hence, the total kinetic energy is decreased. The internal torque generate a heating of the disk.

From eq. (3.23) , the heating for unit time and unit surface is:

$$Q = \frac{G}{2\pi r}\frac{d\omega}{dr}, \tag{3.24}$$

that, using eq. (3.22), is:

$$Q = \frac{3GM\dot{M}}{4\pi r^3}R(r). \tag{3.25}$$

It's worth to highlight that these relations do not depend on the specific nature of the torque.

If we assume that all this energy is radiated away, than integrating on the whole disk (from r_m to ∞), we obtain the total luminosity of the disk:

$$L = \left(\frac{3}{2} - \beta\right)\frac{GM\dot{M}}{r_m}. \tag{3.26}$$

Equation (3.26) explains the high radiative efficiency of an accretion disk. As we have seen in subsection 3.3.1, spherical accretion is radiatively low-efficient: almost all the potential energy is converted in kinetic energy and not in radiation. In an accretion disk, at least (for $\beta = 1$) one half of the potential energy is radiated away, being the other half converted in rotational kinetic energy, according to the virial theorem. Hence, neglecting every relativistic effects, the total radiative efficiency is:

$$\eta \equiv \frac{L}{\dot{M}c^2} = \frac{GM}{2r_m c^2} = \frac{r_{Schwarz}}{2r_m}. \tag{3.27}$$

Since for a Schwarzschild BH $r_m \approx 3r_{Schwarz}$ (Vietri 2006), the efficiency so estimated is 1/6. However an exact calculation that accounts for relativistic effects depends on the BH's spin and can be found in (Vietri 2006).

Knowing Q, we can determine the temperature T and the spectrum of the disk. If we assume following (Vietri 2006) that the disk is in local thermal equilibrium, so that all the heat is dissipated locally:

$$Q = 2\sigma_{SB}T^4 \tag{3.28}$$

where, σ_{SB} is the Stefan-Boltzmann constant. It means that:

$$T = \left(\frac{3GM\dot{M}R(r)}{8\pi\sigma_{SB}r^3}\right)^{1/4}. \tag{3.29}$$

Using equation (3.6), (3.7) and defining $x \equiv r/r_{Schw}$, we can write:

$$T = 8 \times 10^7 K \left(\frac{0.1}{\eta}\right)^{1/4} \left(\frac{L}{L_E}\right)^{1/4} \left(\frac{10^{38}\mathrm{erg\,s^{-1}}}{L_E}\right)^{1/4} \left(\frac{R(x)}{x^3}\right)^{1/4}. \tag{3.30}$$

From the previous equation and from the (3.6), we can see that the higher the black hole mass, the colder its accretion disk.

With the assumption of local thermal equilibrium, we expect that at least locally the spectrum is the one of a black body; hence, the total spectrum is the overlapping of many black body spectrum and:

$$L_\epsilon = 4\pi r_{Schw}^2 \int x dx \frac{2\epsilon^3}{h^3c^2} \frac{1}{e^{\epsilon/kT(x)} - 1}. \tag{3.31}$$

So far, we have not specified the nature of the torque. It has been unknown for a long time, but nowadays it is well understood: it is a magnetohydrodynamic effect.

In magnetohydrodynamics the fluid stress tensor possesses a term due to the magnetic field: the Maxwell stress tensor. The component Mij of the Maxwell stress tensor represents the flux of the $i-$component of the momentum along the direction $\hat{j}$:

$$M_{ij} = -\frac{1}{4\pi}\left(E_i E_j + B_i B_j - \frac{\delta_{ij}}{2}(E^2 + B^2)\right). \tag{3.32}$$

we neglect the terms relative to the electric field, because in astrophysics the electrical conductivity is infinite and $\vec{E} = -\frac{\vec{v}}{c} \wedge \vec{B}$, so they are quadratic in v/c.

$rM_{r\phi}$ is the flux of the component L_z of the angular moment through a surface orthogonal to $\hat{\phi}$, that is the angular moment lost by the material within the radius r, benefiting the material outside the radius r.

Hence, the torque G is:

$$G = \int d\phi r \int dz r M_{r\phi} = \frac{r^2}{2} \int dz B_r B_\phi \tag{3.33}$$

Here a problem arise: in case of hydromagnetic turbulence, B_r and B_ϕ are completely uncorrelated ad hence their average is null: hence there cannot be any loss of angular momentum.

To produce a flux of angular momentum it is necessary that $B_r B_\phi$ is negative along all the lines $r = constant$: this is the result of a magnetohydrodynamical instability, known as BHVC or MRI.

Consider a magnetic field line, oriented along the rotational axis, at distance r_0 from the center: let us suppose that the line immersed in the disk is perturbed in a "S" shape. Since the electric resistance is null the magnetic field is frozen out, so the central point of the S, settled in r_0, continue to rotate with unperturbed velocity, while the curves of the S are settled in regions that rotate faster or slower than r_0. As a result, the line is stretched in a direction that has both radial and tangential components. The shape of the S become always more stressed, while the magnetic field try to rectify it. Distinguishing fours part in the S according to their concavity and convexity, it is found that in each part the sign of the product $B_r B_\phi$ is consistent, showing that there is an outward flux of angular momentum.

Having described the main features of an accretion disk, before to end this section we want to highlight some observations.

First of all, eq.(3.30) shows that stellar mass BHs have accretion disks that emit mainly in the X-ray band. The accretion disks of supermassive black holes of masses of order $10^9 M_\odot$, instead, have the maximum of the emission in the UV band; nevertheless, observations show that the environments that surround

SMBHs are also characterized by a strong emission in the X-ray band.

Since the origin of the energetic X-ray photons cannot be the disk itself, it is likely that their source is a hot medium in the proximity of the disk. The scientific community agree that the soft disk emitted photons could be upscattered to their observed X-ray energy through inverse Compton effect in a hot, diluted gas called *corona*. The conditions for the formation of a hot corona around a thin accretion disk are still unknown, although there are some interesting hypothesis that involve an high density gradient in the disk accretion and the heating of the outer layers through both the radiation from the disk and strong magnetic fields. Figure 3.2 shows two possible locations of the corona: the right side of the pictures involves a disk-corona structure in which the corona photons can irradiate the disk, changing the local energy balance. This possibility complicates the physics of the disk, that will not be described here.

Figure 3.2: Two schematic diskcorona structures showing possible locations of the corona and the scattering geometry of the disk-produced and corona-produced photons, by (Netzer 2013).

We conclude this section stressing that, in order to predict an AGN spectrum, we need to take into account that, in their travel throughout the host galaxy, the photons produced in a SMBH's environment have some probability to interact with the interstellar medium and hence to be absorbed or scattered away. Since this work is focussed on the visibility of quasars in the X-ray band, we will concentrate on the main processes that determine an attenuation of the flux emitted in the this band: the Compton effect and the photoelectric effect (being the energy of the X-ray photons higher of the ionization energy of the atoms, we will assume that the photoelectric absorption occurs with the extraction of an electron from the K-shell of the atom (Morrison and McCammon 1983 and Yaqoob 1997).

Going through a material with number density n for an infinitesimal path dl, the number of photons in a beam N change as: $dN = -Nn\sigma dl$, where σ is the total cross-section for the attenuation processes. Hence, the photons that survive after having travelled along a line of sight are:

$$N = N_0\, e^{-\int n\,\sigma\, dl} = N_0 e^{-\tau}, \tag{3.34}$$

where τ is a key quantity in astrophysics and is called *optical depth*.

4 Faint progenitors of luminous quasars

In this chapter we will introduce the scientific issue that underlies this work: it concerns the formation and the growth of the supermassive ($\sim 10^9 M_\odot$) black holes (SMBHs) that power high-redshift active galactic nuclei (AGNs). Several models have been theorised to explain the existence of such massive objects less than one billion years after the Big Bang, when galaxies were in their infancy: some models explore the possibility that these enormous objects form by accretion on smaller BHs, others call for the gradual merging of stellar-mass or intermediate-mass black holes, the *progenitors*.

Section 4.1 is a brief introduction to the problems of the SMBHs' formation and growth. Then, in section 4.2, we will describe the theoretical models related to the collapse and the formation of BHs of stellar and intermediate mass. In section 4.3 we will introduce the outstanding issues related to the accretion and present the merging theory. Finally, in section 4.4 we will describe the "merger tree" method, that allow us to study hierarchical models in which SMBHs form by merging.

4.1 The problem

In chapter 3, we illustrated the current paradigm that explains the central engine of these bright non-stellar sources, known as quasars, observed in our universe. However, the detection of high-redshift quasars poses several other questions concerning their birth, growth and evolution.

The most distant quasar currently known, ULAS J1120+0641 (Mortlock et al. 2011), has a redshift z = 7.085, corresponding to less than 800 millions years after the Big Bang.

Following Petri et al. 2012, if we assume that the BH accretes a mass fraction

$(1-\eta)$ at the Eddington rate (see section 3.3), its growth can be described as:

$$\frac{d\ln M}{dt} = \frac{1-\eta}{\eta}\frac{1}{t_E} \tag{4.1}$$

where $t_E \approx 0.45$Gyr is the Eddington time defined in section 3.3. Thus:

$$M(z) = M_0 e^{\frac{1-\eta}{\eta}\frac{t(z)}{t_E}}. \tag{4.2}$$

Hence, for the usually assumed value of the radiative efficiency $\eta = 0.1$, ULAS J1120+0641 requires an initial *seed* (i.e. the initial black hole of mass M_0, that is the starting point from which a SMBH can form) with mass $M_0 \geq 500 M_\odot$ [1] to achieve a mass $M = 2 \times 10^9 M_\odot$ (Mortlock et al. 2011) at $z \sim 7$: a value that is much larger with respect to the mass $M_{stars} < 100 M_\odot$ estimated for the first stars (Greif et al. 2011). Furthermore, it is not realistic to assume that accretion occurred at its maximum value (the Eddington rate) for almost 1 Gyr.

This example highlights two main outstanding issues concerning the high-redshift quasars central BHs:

- the nature and the formation of their *seeds*,
- the mechanisms through which the *seeds* accrete up to the huge mass of a SMBH.

We will discuss the first issue in sec. 4.2 and the second one in sec. 4.3.

4.2 Seed formation models

In this section, we will focus on the SMBHs' seeds and in particular on the theoretical models developed to describe their formation. Approximately the seeds can be distinguished (Volonteri 2010) in:

- *light* seeds ($M \approx 10^2 M_\odot$), formed in the very early universe ($z \simeq 20 - 50$),
- *intermediate* seeds ($M \approx 10^3 M_\odot$), formed between $z \simeq 10 - 15$.
- *heavy* seeds ($M \approx (10^4 - 10^6) M_\odot$), formed between $z \simeq 5 - 10$,

According to theoretical models, light seeds form very early, hence, in principle, they have more time to grow and to merge; nevertheless, their accretion rate is

[1] the value $500 M_\odot$ is a lower boound, in fact it has been calculated as if the time available for accretion was 0.77 Gyr, the age of the universe at $z = 7$.

lower, especially in presence of its own radiative feedback. On the other hand, heavy seeds have less time to grow, but this can be compensated by they higher initial mass.

Current observations do not allow us to understand if one of these initial conditions is favourite: we rely on future high-redshift observations performed by the next generation of telescopes, such as the James Webb Space Telescope (JWST).

In this work, we will briefly describe two main hypothesis: that the SMBHs' seeds are the result of a direct gravitational collapse and that they are *remnants* of massive stars, These formation models will be the main topic of the subsections 4.2.2 and 4.2.1.

4.2.1 Direct collapse

In this chapter we will introduce the direct collapse process. This model of BHs' formation was introduced to solve the problem of the SMBHs' seeds nature and predicts that, under specific conditions, compact objects of mass up to $10^6 M_\odot$ can form directly through general relativity (GR) instabilities.

In order to explain the conditions needed for a direct collapse black hole (DCBH) to form, we need to analyze the cooling processes that occur in astrophysical environments. In a non-ionized gas cloud (it is indeed the case if the temperature T is lower than $10^5 \div 10^6$ K), the cooling channels are essentially three:

- if heavy elements are present in a fraction $M_{metals}/M_{gas} > 10^{-4}$, they dominate the cooling through processes as dust thermal emission, molecular and atomic line emission.

- If the gas is pristine (i.e. metal-free), the cooling proceeds through the relaxation of the H_2 rotational bands: the minimum temperature above which this cooling channel is enabled is $T_{H_2} = 10^2 \div 10^3$ K. Anyway the H_2 molecule is rather fragile: if the background flux in the $Lyman-Werner$ band (11.2-13.6 eV) is strong enough (order of $10^{-18} \div 10^{-16}\,\mathrm{erg\,cm^{-2}\,s^{-1}\,Hz^{-1}}$, from Bromm and Loeb 2003), it breaks and the cooling process is realized only through atomic hydrogen.

- The cooling of a pristine atomic gas cloud is executed mainly by the Lyman$-\alpha$ emission of the neutral H, that takes place for a minimum temperature $\approx 10^4$ K.

Numerical simulations suggest that there are three precise conditions to be simultaneously satisfied for the direct collapse to occur:

- the halo must be pristine: the consequences of the presence of metals has been studied by Omukai et al. 2008 performing numerical simulations; according to their results, for metallicities above 10^{-4}, cooling induces fragmentation in pieces of mass $\sim 0.1 M_{\odot}$.
- The halo must be massive enough for the cooling to be dominated by the atomic H, hence is virial temperature must be $T_{vir} > 10^4$ K.
- The Lyman-Werner background must be strong enough for the H_2 cooling to be inhibited, so that no fragmentation (and so star formation) can occur. In fact, efficient gas collapse leading to a massive black hole seed formation is mutually exclusive with star formation, as the competition for the gas supply limits the collapsing mass available.

Under these conditions, the baryons stream toward the center and it is possible that they enter a GR instability that leads to the formation of a DCBH.

DCBHs are a fascinating and popular solution to the problem of the seeds formation; nevertheless, at the present time it is only a theoretical scenario that has not been observationally confirmed yet.

4.2.2 Massive star remnants

One of the most popular scenarios for the formation of SMBHs associates their seeds to the remnants of the older generations of stars. Astronomers distinguish three population of stars by their abundance of heavy elements:

- *population I (popI)* stars includes the Sun and are the most rich in metals. According to the models for formation of heavy elements, they are likely to be formed out by the gas contaminate with the heavy elements formed by previous giant stars. Since they are generally settled in low redshift galaxies, popI stars are not likely to form high-redhift SMBHs' seeds.
- *Population II (popII)* stars are generally settled in high-redshift galaxies. Their main feature is the low metal contents, due to the fact they formed in regions with no heavy-element pollution. Since popII stars can be massive, they could be good candidates for the formation of the SMBHs' seeds.

- *population III (popIII)* stars are predicted to form by pristine gas and are completely metal-free. We saw in the last subsection that above a certain temperature threshold the H_2 time is shorter than the Hubble time at virialization and stars can form. Simulations of the collapse of primordial molecular clouds Carr et al. 1984 suggest that the first population of stars was also very massive ($M_* > 100 M_\odot$). Anyway, even if the popIII stars' remnants would be good candidate for the formation of SMBHs' seeds, their existence has not been confirmed yet, but see Sobral et al. 2015 for recent claims of observations.

Very massive stars have an estimated lifetime of order of million years and their end depends mainly on the value of their mass:

- $25 < M_*/M_\odot < 140$. In this mass range, a metal free star is predicted to form directly a BH. Nevertheless the resulting BHs are predicted to be too light to settle at the center of the host galaxy potential well and may be wandering within the host. Hence, stars in this range of masses are not predicted to leave a SMBHs' seed.

- $140 < M_*/M_\odot < 260$. Theoretical models predict that in the core of massive stars within this range, after the central He burning, electron-positron pairs are produced in abundance. The loss of this radiative energy (called pair-instability) causes a decrease of the radiation pressure and a violent collapse of the star under its own gravity, until O and Si burning produce enough energy to reverse the collapse. This kind of stars are not supposed to produce BHs, since the nuclear-powered explosions completely destroy them and leave no remnants (references).

- $M_*/M_\odot > 260$. In this mass range, a star is not affected from the instability described in the previous point and it can collapse in a black hole without destructive explosions. The BHs produced in this case have masses intermediate between those of the stellar and the supermassive variety, then the final destiny of a star in this case could be to form a SMBH seed.

To conclude this section, we comment that remnants of very high redshift massive stars can give life to SMBHs' seeds, but their mass is likely to be of order $10^2 M_\odot$, and we still need to understand if these light seeds can grow up to the huge mass of a SMBH.

4.3 The growth problem

Assuming that a black hole seed forms at $z = 20$, the simple calculation in sec. 4.1 tells us that, if it starts from a mass that is at least $10^2 \div 10^3 M_\odot$, it could reach a mass of order $10^7 \div 10^8 M_\odot$ at $z = 7$, provided that it accretes always at the Eddington rate (eq. (3.8)). Anyway, there is no a well justified reason to assume that a black hole accretes at the maximum accretion rate all its life long: this scenario is not explained by numerical simulations.

Some authors, for example Willott et al. 2010, studied the possibility of the formation of SMBHs starting from small ($M < 100 M_\odot$) seeds, provided they experience several mergers and periods of super-Eddington accretion. Current observations support the fact that sporadic events of super-Eddington accretion can occur at $z \sim 6$: in these conditions, low mass seeds can still generate a SMBH. Others, for example Petri et al. 2012, explored the possibility that the growth occurs through merging of heavier seeds.

In the subsection 2.2.5 we explained that the structure formation through the growth of perturbations in the cosmic density field occurs $bottom - up$: smaller structures form first and, gradually, the formation of more massive structures takes place. The detection of high redshift interacting galaxies highlights the possibility that the DM halos supposed to embed low-redshift galaxies could be formed by merging of two already virialized halos. We expect that the hierarchical build-up of galaxies through mergers could produce black hole binaries that tighten because of the dynamical friction with the background gas and finally coalesce. Some authors (e.g. Berti et al. 2006) claimed that, with our current experimental instruments, we can hope to identify SMBHs' seeds during their mergers by their gravitational-wave emission predicted by general relativity.

From the theoretical side, the study of the merging of virialized haloes can be done with the mass function formalism described in the subsection 2.2.5: the probability distribution function in eq.(2.59) of chapter 2 can be converted to a Monte Carlo code through a computational procedure that, given a DM halo at a given z, simulates its statistical merger history. This method is the main topic of the next section.

4.4 The Merger-Tree method

In subsection 2.2.5 we described the PS formalism and mention the extended PS formalism from which we can obtain equation (2.59).

Given an halo of mass and redshift (M_1, z_1) the extended PS formalism allows us to know the mass distribution of the progenitors at some redshift $z_2 > z_1$.

In the limit $z_2 \to z_1$ (i.e. for a small redshift interval Δz), one can write:

$$\frac{dN}{dM_2}(z_2 \to z_1) = \frac{M_1}{M_2^2}\frac{df_{PS}(\nu_{12})}{dz_2}\left|\frac{d\ln\nu_{12}}{d\ln M_2}\right|\Delta z \tag{4.3}$$

that is proportional to the mean number of progenitors of mass M_2 in which the parent halo of mass M_1 is split when a step redshift $z_1 \longrightarrow z_2 = z_1 + \Delta z$ is taken. Lacey and Cole 1993 exploited these results to develop a computational approach to study hierarchical models in which structures grow through gravitational instabilities: the *merger tree method*.

This approach is based on an algorithm that can be used to reconstruct sort of a genealogical tree of a SMBH: considering a DM halo of mass M_1 at $z = z_1$ hosting a SMBH, the algorithm proceeds backward in time reconstructing its statistical merger history, accounting at each step that the halo can be split in two progenitors or not.

To construct the numerical algorithm essential to simulate $\frac{dN}{dM_2}$, one needs to fix a mass resolution M_{res} to keep the computational time reasonable (all detail of $M < M_{res}$ are ignored). Lacey and Cole 1993 defined the mean number of progenitors, P, and the mass fraction of the final object in progenitors of mass smaller than M_{res}, F:

$$P = \int_{M_{res}}^{M_1/2}\frac{dN}{dM_2}dM_2, \tag{4.4}$$

$$F = \int_0^{M_{res}}\frac{dN}{dM_2}\frac{M_2}{M_1}dM_2 \tag{4.5}$$

Setting the initial condition (M_1, z_1) we go backward in time of a redshift interval Δz small enough to ensure that the splitting is at most binary (i.e. $P \ll 1$). Then a number $0 < R < 1$ is generated and is compared to P:

- if $R > P$, the halo does not split in two parents and its mass at redshift $z_1 + \Delta z$ is $M_1(1 - F)$, i.e. the ignored details below M_{res} are assumed to be accreted mass in the time interval corresponding to $-\Delta z$.

- if $R \leq P$, the halo split in two progenitors: one of mass M_2 (randomly generated in the mass interval $M_{res} < M_2 < M_1/2$) and one of mass $M_1(1 - F) - M_2$.

This procedure is iterated for every new generated halo, at increasing z, gen-

erating the merger tree. Thus, in the description of a merger tree algorithm, we need to specify the following parameters: $M_{res}, \Delta z, z_1, z_{end}, M_1$. In figure 4.1 is represented an example of merger tree.

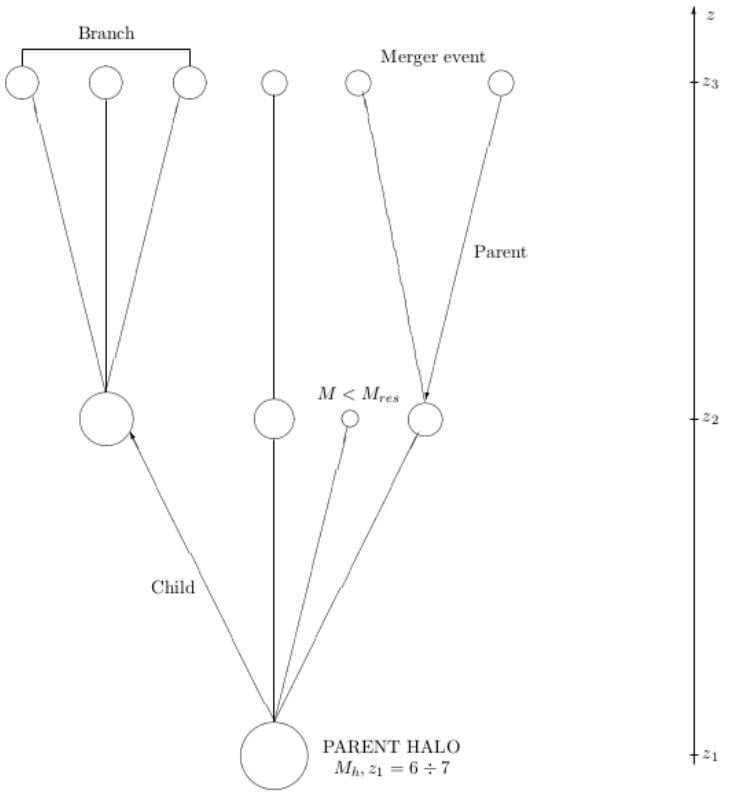

Figure 4.1: Example of merger tree with 3 levels and 11 nodes. In the figure, the "parent" halo splits in 3 progenitors of $M > M_{res}$ at redshift z_2 (courtesy of A. Petri, master thesis).

5 A simple model for the X-ray spectrum

In the last chapter, we introduced the scientific issue that concerns the supermassive black holes (SMBHs) formation and the theoretical models developed in order to solve it. Among them, we considered the possibility that these powerful objects form by merging of smaller black holes, besides accreting material falling into the black hole.

Having the chance to detect the SMBHs' ancestors would be a remarkable observational breakthrough and would give cosmologists the opportunity to improve our knowledge on the birth and evolution of these mysterious objects and their host galaxies and to better constrain the theory.

Several detection attempts have been done with the most powerful observatory available at the moment, the Chandra X-ray Observatory, but no positive responses have been obtained at the present time.

In the following two chapters we will try to understand if our current technologies are sensitive enough to detect such sources. In particular we will investigate: (*i*) if they are very faint (for example because they could be buried in a blanket of obscuring material) and need more sensitive tools to be observed; (*ii*) if they are very rare and we should explore larger regions of the sky to increase the detection probability.

The aim of this chapter is to model the radiative X-ray flux density of an accreting black hole (BH) and the following absorption from the obscuring material that surrounds the source; this emission model will be applied to the accreting high-redshift black holes simulated with a merger tree by Valiante et al. 2011, in order to estimate the X-ray luminosity expected for the SMBHs' ancestors.

In sec. 5.1 we will describe in details the data that the merger tree by Valiante et al. 2011 provide us. Then, in sec. 5.2 and 5.3, we will describe the emission and the absorption model, respectively, and we will make a prediction on the expected SMBHs' ancestors luminosity in the X-ray band.

5.1 Data from the Merger-Tree - GAMETE/QSO$_{\rm DUST}$

Valiante et al. 2011 developed a semi-analytical model for the formation and evolution of high-z quasars, in order to study the origin of dust in these objects. In particular, they studied the case of a dark matter halo of $M_h = 10^{13} M_\odot$ at $z = 6.4$ and compared their results with the observational features of the quasar SDSS J1148+5251, powered by a BH of mass $M_{BH} \approx 3 \times 10^9 M_\odot$, detected at $z = 6.4$ Willott et al. 2003.

Their code (GAMETE/QSO$_{\rm DUST}$) consists of two blocks: the first one runs backward in time and stochastically reconstructs the merger tree of the assumed $10^{13} M_\odot$ dark mater halo at $z = 6.4$; the second runs forward in time and allow them, thanks to an analytical model, to follow the evolution of the baryonic component of the halo and the growth of the central BH.

The first block of their code is based on a merger tree with the following characteristics (see section 4.4 for the meaning of each quantity):

- a redshift dependent resolution mass $M_{res}(z) = 10 M(T_{vir} = 10^4 K, z)$, being $M(T_{vir} = 10^4 \mathrm{K}, \mathrm{z})$ the mass of a DM halo with a virial temperature of 10^4 K (eq. (2.48)) at redshift z;
- 5000 redshift intervals logarithmically spaced in the expansion factor between $z = 6.4$ and $z = 37$.
- a BH seed of mass $M_{seed} = 10^4 h^{-1} M_\odot$ assigned to all the progenitor halos corresponding to density fluctuation higher than $4 - \sigma$ ($M > M_{4-\sigma}$) that exceed the threshold mass required to form stars ($M > M_{sf}$) for the first time in the merger tree.

Here we briefly present in detail the (Valiante et al. 2011) data that we are going to use in the next parts of the chapter.

We will use four sets of data, corresponding to two different models (labelled as B1 and B3), at two different redshifts ($z = 7$ and $z = 8$). Each of the four data sets contains the accretion rate in $M_\odot$/yr for each progenitor, the hydrogen column density in cm^{-2}, the metallicity (ratio of the metals mass to the total gas mass) and the ratio of the dust mass to the total gas mass for its surrounding environment.

The two models differ for the prescriptions used for star formation history (SFH), star formation efficiency and initial mass function (IMF):

	Model B1	Model B3
$z = 7$	8.3×10^{-4}	6.4×10^{-4}
$z = 8$	3.4×10^{-4}	2.8×10^{-4}

Table 5.1: Average accretion rates (in $M_\odot/yr$) for models B1 and B3 at $z = 7$ and $z = 8$. It is worth to notice that the average accretion rate at redshift $z = 8$ decrease of a factor ≈ 2 with respect to $z = 7$ in both models.

- the SFH is the time distribution of the star formation occurred in the halo. In GAMETE/QSO$_{\rm DUST}$ it is decomposed in a continuous and a bursty components; In the models B1 and B3 the bursty component dominates.
- the star formation efficiency is the fraction of baryons in the galaxy that is in stars. The model B1 has a lower star formation efficiency than the B3.
- the IMF $\phi(M)dM$ is the probability that a newly formed star has a mass between M and $M + dM$.

Both models assume that stars form according to a Larson IMF (Larson 1998):

$$\phi(m) \propto m^{-\alpha} e^{-\frac{m_{ch}}{m}} \tag{5.1}$$

where $\alpha = 2.35$ is the Salpeter power law index Salpeter 1955, but differs for the value of the parameter m_{ch} that is $5M_\odot$ in model B1 and $0.35M_\odot$ in model B3; the trend of the Larson IMF for this two different values of m_{ch} is shown in figure 5.1: a larger value of m_{ch} shifts the maximum of $\phi(m)$ to a larger value of the stellar mass.

In the following, for brevity, we will show only to the details obtained for the B1-set of data, where they are analogue to the ones obtained using model B3. We will highlight the differences with some comments, where there is any.

Figure 5.2 shows the probability distribution function (PDF) normalized to unity of the BH accretion rates, for model B1 at $z = 7$, while the numerical values of the average accretion rates for each data set are shown in table 5.1. In both models B1 and B3 the accretion rates vary from $10^{-7} M_\odot/yr$ to $10^2 M_\odot/yr$ (with an average accretion rate that is slightly higher for the model B1) and there is a decrease of a factor ≈ 2 of the average accretion rate at redshift $z = 8$ with respect to $z = 7$.

We call *quiescent* (*active*) a SMBH if the luminosity produced by its accretion is less (greater) than the typical luminosity of a galaxy, that we will assume to be $L_{galaxy} \approx 10^{11} L_\odot \approx 4 \times 10^{44} erg/s$. Then, assuming a radiative efficiency $\eta = 0.1$, equation (3.9) suggests that a quiescent BH should have a mass accretion rate

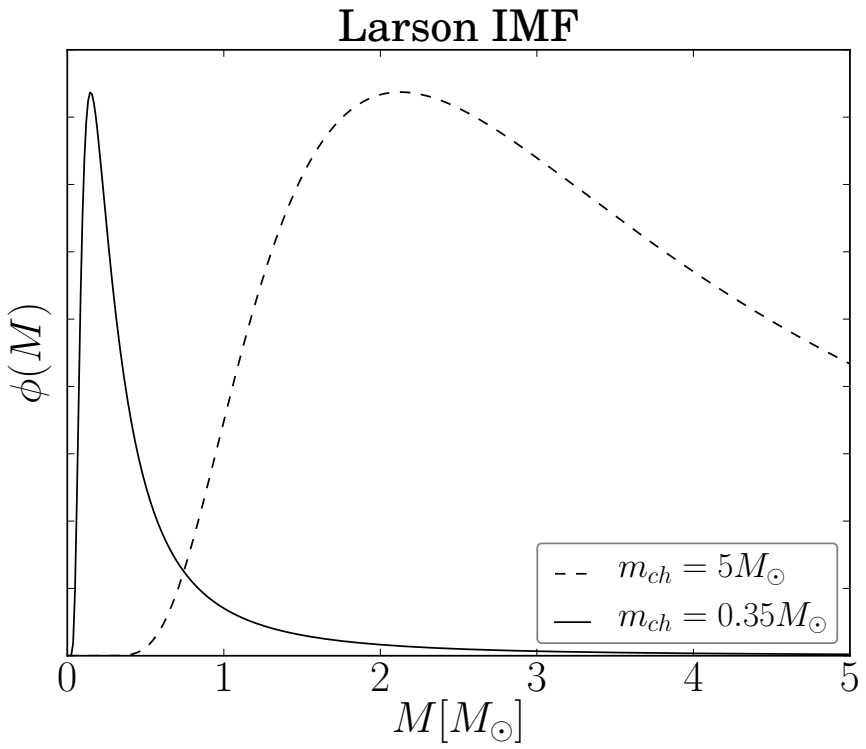

Figure 5.1: Trend of the Larson IMF for the two different values of m_{ch} that discriminate models B1 and B3. As is shown the larger value of m_{ch} shifts the maximum of $\phi(M)$ to a larger value of the stellar mass. Each $\phi(M)$ is expressed in arbitrary units.

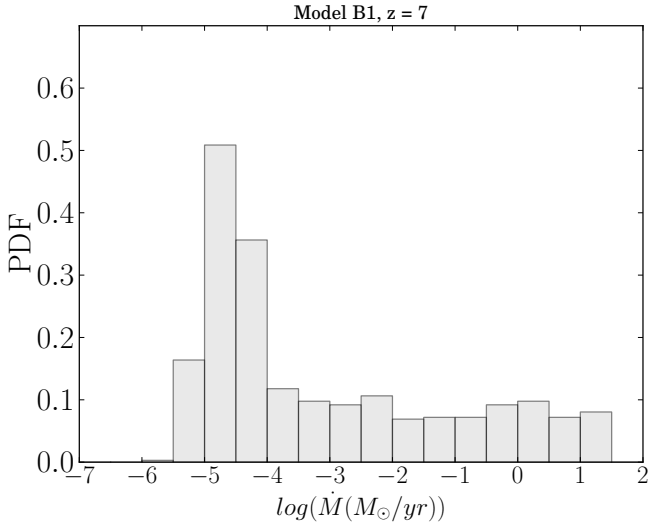

Figure 5.2: Probability distribution function of the mass accretion rates $\dot{M}_{BH}$ of the black holes simulated by Valiante et al. 2011 for their model B1 at $z = 7$. With a quick glance at the picture we can see that the majority of the simulated progenitors are *quiescent* (i.e. have $\dot{M}_{BH} \leq 6 \times 10^{-2} M_\odot/yr$) and only a minor fraction is *active* (i.e. have $\dot{M}_{BH} > 6 \times 10^{-2} M_\odot/yr$).

	Model B1	Model B3
$z = 7$	0.77	0.89
$z = 8$	0.79	0.91

Table 5.2: Fraction of progenitors that present an accretion rate lower than $6 \times 10^{-2} M_{\odot}/yr$ for models B1 and B3 at $z = 7$ and $z = 8$. The progenitors at $z = 8$ are characterized by a more quiescent fraction and progenitors simulated according to the model B1 are characterized by a higher active fraction.

$\dot{M}_{BH} \leq 6 \times 10^{-2} M_{\odot}/yr$. According to figure 5.2, the majority of the simulated progenitors are *quiescent* and only a minor fraction is *active*. In table 5.2 is listed the fraction of quiescent progenitors for the two models and the two redshifts: progenitors simulated according to the model B1 are characterized by a higher accretion activity.

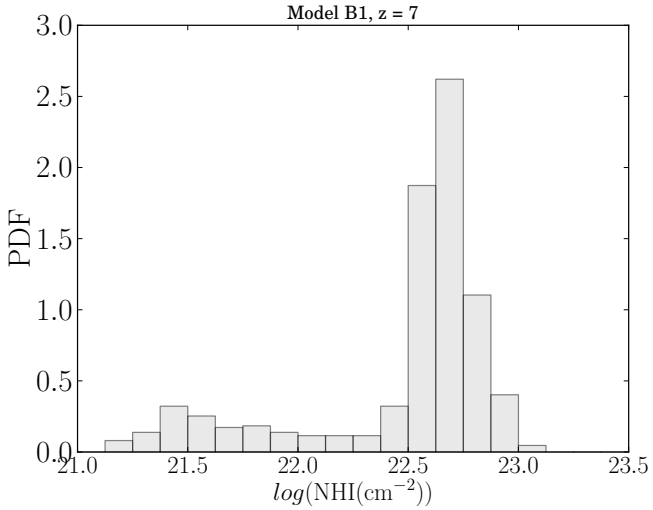

Figure 5.3: Probability distribution function of the column densities N_{HI} simulated by Valiante et al. 2011 for their model B1 at $z = 7$. No one of the progenitor is surrounded by a Compton thick ($N_{HI} \sim {\sigma_T}^{-1} = 1.5 \times 10^{24} \mathrm{cm}^{-2}$) environment.

Figure 5.3 shows the probability distribution function (PDF) normalized to unity of the BH neutral hydrogen column densities N_{HI}, for model B1 at $z = 7$. Table 5.3 reports the average column densities for the two models at the two redshifts. $z = 8$ progenitors are covered by a hydrogen blanket that is the 20% more dense with respect to the ones at $z = 7$. Furthermore the B1 model generated progenitors more obscured than in model B3.

It's interesting to note that no one of the environments simulated by Valiante et al. 2011 is *Compton-thick*, that is none has a column density higher than $N_{HI} \sim {\sigma_T}^{-1} = 1.5 \times 10^{24} \mathrm{cm}^{-2}$, where $\sigma_T = 6.6 \times 10^{-25} \mathrm{cm}^2$ is the Thomson cross-section (Comastri 2004).

Finally, figure 5.4 shows the PDF normalized to unity of the metallicity and

	Model B1	Model B3
$z = 7$	3.0×10^{22}	2.7×10^{22}
$z = 8$	3.7×10^{22}	3.2×10^{22}

Table 5.3: Average column densities (in cm^{-2}) for models B1 and B3 at $z = 7$ and $z = 8$. $z = 8$ progenitors are covered by a hydrogen blanket that is the 20% more dense with respect to the ones at $z = 7$. Furthermore the B1 model gener ated progenitors more obscured than in model B3.

the dust to gas ratio in the environment around the simulated progenitors. In particular, figure 5.4a shows that a very small fraction of the simulated BHs is surrounded by an environment with metallicity higher or equal to the solar value $Z_\odot = 0.0122$ (Asplund et al. 2009), being $\log Z_\odot \approx -2$.

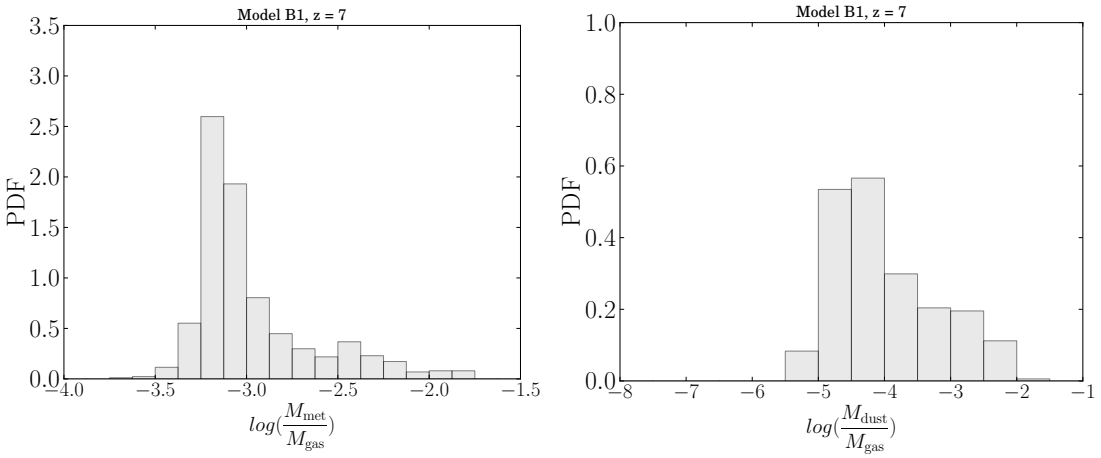

(a) Metallicity **(b)** Dust to gas ratio

Figure 5.4: These figures show on the left (right) the probability distribution function of the metallicities (dust to gas ratios) simulated by Valiante et al. 2011 for their model B1 at $z = 7$.

To conclude the description of the data that we will use, we want to understand if there are some relation between the simulated properties of the progenitors (accretion rate, hydrogen column density, metallicity and dust ratio). As representative case we will show the results for model B1 at $z = 7$ only. In figure 5.5 we report the scatter plot of the mass accretion rate versus the hydrogen column density and the dust to gas ratio. The scatter plots of the other four possible coupling of the four quantities do not reveal any strong correlation among them.

As is shown in figure 5.5a the simulated progenitors can present a high, $(10^{-2} \div 10^{2}) M_\odot/yr$, accretion rate in the whole range $(10^{21} \div 10^{23})\mathrm{cm}^{-2}$ of hydrogen column densities. However, more than a half of the progenitors lies in correspondence of low ($\dot{M}_{BH} < 10^{-2} M_\odot/yr$) accretion rates and column densities $N_{HI} > 10^{22}\mathrm{cm}^{-2}$, while it can be noticed that very few progenitors (and, in some

models, none) present at the same time very low accretion rate and very low column density.

The direct correlation between the dust to gas ratio and the mass accretion rate appears more well-defined: according to figure 5.5b there are not active progenitors with low dust to gas ratio ($\frac{M_{dust}}{M_{gas}} < 10^{-4}$) and there are not quiescent ones with high dust to gas ratio.

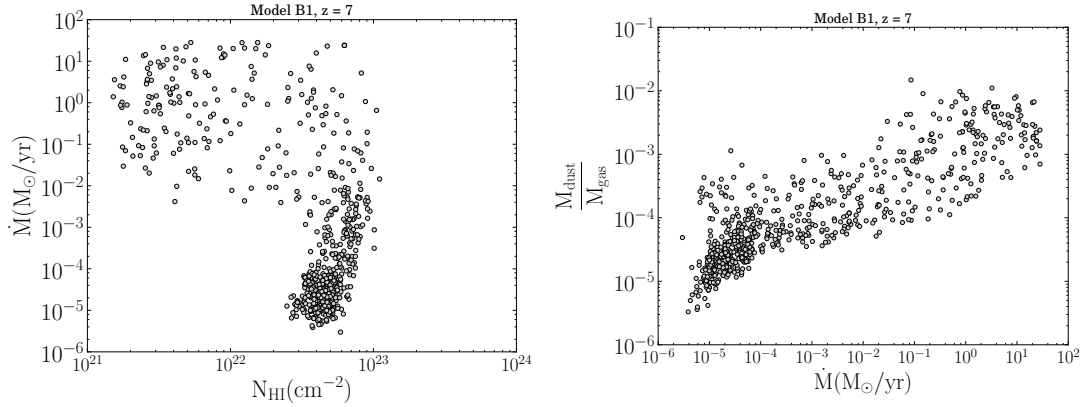

(a) Accretion rate vs column density

(b) Accretion rate vs dust to gas ratio

Figure 5.5: Correlation between the mass accretion rate and the other quantities simulated by Valiante et al. 2011 . (a) More than a half of the progenitors lies in correspondence of low accretion rates and high column densities. (b) There is a well-defined direct correlation between the dust to gas ratio and the mass accretion rate.

5.2 The intrinsic flux density

In chapter 3 (section 3.3) we noticed that accretion on a BH is an efficient mechanism for producing electromagnetic radiation. The generated luminosity is usually parametrized in terms of the dimensionless radiative efficiency η:

$$L_{bol} = \dot{M}_{BH} \frac{\eta c^2}{1-\eta} \tag{5.2}$$

We have already highlighted in section 3.3 that the estimation of realistic values of η is an important and problematic issue: we remind our choice to assume the standard value in literature (e.g. Vietri 2006, Petri et al. 2012, Volonteri and Stark 2011 and Frank et al. 2002) $\eta = 0.1$, as fiducial value. Thus, according to (5.2), $L_{bol}(\dot{M}_{BH}) = 6.4 \times 10^{45} \left(\frac{\dot{M}_{BH}}{1 M_\odot/\mathrm{yr}}\right) \mathrm{erg} \cdot \mathrm{s}^{-1}$.

Since the luminosity L_{bol} is the sum of the optical-ultraviolet and the X-ray luminosities radiated by the accretion disk and the hot corona, respectively, we

need to apply suitable bolometric corrections to L_{bol} in order to estimate the luminosity in both the soft and the hard X-ray bands.

The employed bolometric correction (Marconi et al. 2004) is expressed by the luminosity dependent relations:

$$\log[L/L(2-10\mathrm{keV})] = 1.54 + 0.24\tilde{\mathrm{L}} + 0.012\tilde{\mathrm{L}}^2 - 0.0015\tilde{\mathrm{L}}^3 \tag{5.3}$$

$$\log[L/L(0.5-2\mathrm{keV})] = 1.65 + 0.22\tilde{\mathrm{L}} + 0.012\tilde{\mathrm{L}}^2 - 0.0015\tilde{\mathrm{L}}^3 \tag{5.4}$$

where $\tilde{\mathrm{L}} = (\log L - 12)$ and L is the bolometric luminosity in units of $L_{\odot}$.

The X-ray emission can be modeled as a single power law:

$$F_{\nu} = F_{0_{\nu}} \left(\frac{\nu}{\nu_0}\right)^{-\alpha} \tag{5.5}$$

where the intrinsic flux density F_{ν} is related to luminosity through the relation:

$$F_{\nu} = \frac{(1+z) f_{\nu} L}{4\pi d_L(z)^2}, \tag{5.6}$$

$d_L(z)$ is the redshift dependent luminosity distance defined in section 2.1.1 and f_{ν} is the chosen bolometric correction, normalized according to eqs. (5.3) and (5.4).

Our fiducial value $\alpha = 0.9 \pm 0.1$ for the slope of the X-ray spectrum is derived from the analysis of the XMM-Newton spectra of 40 quasars at redshift $z \leq 1.72$ performed by Piconcelli et al. 2005.

In figure 5.6 it is shown the X-ray intrinsic flux density of a BH that is accreting $1 M_{\odot}$/yr; the shaded region represents the range of the values permitted for the flux density if the slope α varies between $(-3, +3)\sigma$ around the fiducial value $\alpha = 0.9$.

5.3 Absorption from obscuring material

As noticed in section 3.3.2, the radiation produced in the immediate surroundings of a BH has a certain probability to interact with the gas and dust in its environs. In particular, the two main attenuation processes are the photoelectric absorption and the Compton scattering of a photon against a free electron.

The attenuated radiative flux, after the interaction with matter, is:

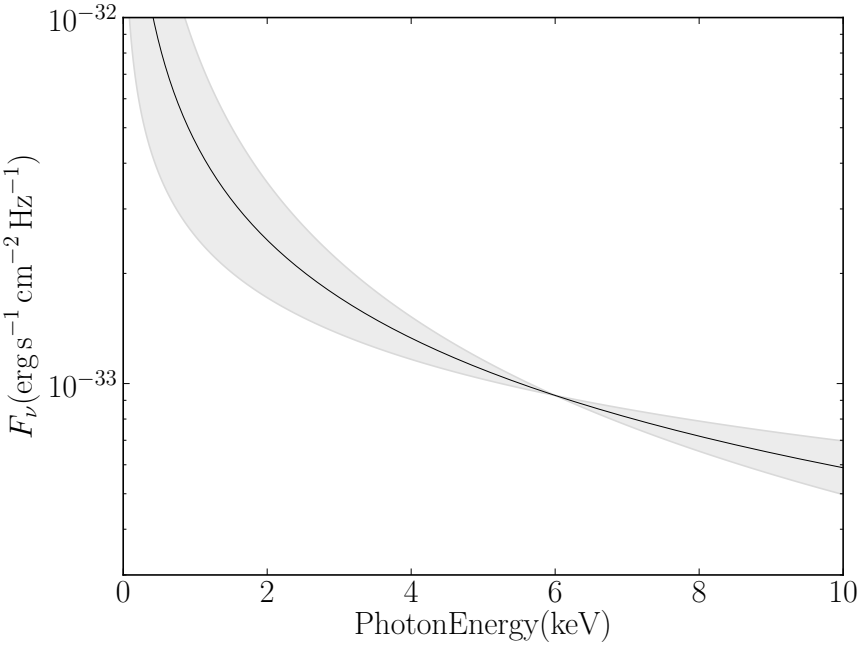

Figure 5.6: Intrinsic flux density evaluated for a BH that is accreting $1M_\odot$/yr. The black line represents the plot arising from the fiducial value of $\alpha = 0.9$ from Piconcelli et al. 2005, while the shaded region spans over the values that the flux density takes between $\alpha \pm 3\sigma$. Since the shaded region depends only on the parameter α, we put it arbitrarily to zero at 6 keV.

$$F_\nu^{obs} = F_\nu e^{-\tau}, \tag{5.7}$$

where $\tau = (1.2\sigma_T + \sigma_{ph})N_H$ is the total optical depth (Yaqoob 1997), as defined in section 3.3.2, N_H is the hydrogen column density, σ_{ph} is the photoelectric cross section and σ_T is the Thomson cross-section.

The factor 1.2 in the previous equation is justified as follows: if we assume that the whole helium is double ionized at the energies in play (assumption well motivated because the He second-ionization potential is about 0.05 keV and we are considering photons in the X-ray band), then the number of free electrons in the gas will be the number of hydrogen atoms plus twice the number of helium atoms:

$$n_{e^-} = n_H + 2n_{He} = n_H(1 + 2\frac{n_{He}}{n_H}) \simeq n_H(1 + \frac{Y}{2X}), \tag{5.8}$$

being X (Y) the ratio of the hydrogen (helium) mass to the total mass gas, $n_{He} = \frac{M_{He}}{\mu_{He} m_u} \approx \frac{Y\,M_{gas}}{4mp}$, $n_H = \frac{M_H}{\mu_H m_u} \approx \frac{X\,M_{gas}}{mp}$, and μ_H , μ_{He} the atomic weight of H and He respectively and m_u the atomic mass unit.

For a primordial universe, where the values for X and Y are esteemed to be around $X \approx 0.76$ and $Y \approx 0.24$, $n_{e^-} \simeq 1.16 n_H$; but since stars are supposed

to produce helium and heavier elements, it is reasonable to assume that these primordial values are lightly modified: assuming a solar-like $X = 0.70$ and $Y = 0.30$, then $n_{e^-} \simeq 1.21 n_H$. Hence, we adopt $n_{e^-} = 1.2 n_H$ as fiducial value, in agreement with Yaqoob 1997. However, this choice does not affect our results: we calculated that the contribution of the Compton effect to the total optical depth is about 0.2% at both 1 keV and 10 keV.

Morrison and McCammon 1983 computed an interstellar photoelectric absorption cross section as a function of energy in the range $(0.03 \div 10)$ keV, for metallicity $Z_\odot^{1982} = 0.0263$, that in 1982 was estimated to be the metallicity of the Sun. [1]

As we discussed (see figure 5.4b), the values of metallicity simulated by Valiante et al. 2011 span a wide range of values: thus, we need to obtain a metallicity dependent cross section. To this purpose, we will break the photoelectric cross section in three terms, expressing the contribution of hydrogen, helium and metals atoms, respectively:

$$\sigma_{ph} = \sigma_H + \sigma_{He} + \sigma_{metals}. \tag{5.9}$$

The only term in the previous equation that depends on metallicity is σ_{metals}; therefore if we compute σ_H and σ_{He}, we can obtain σ_{metals}^{MMCC} for the metallicity used by Morrison and McCammon 1983:

$$\sigma_{metals}^{MMCC} = \sigma_{ph} - (\sigma_H + \sigma_{He}). \tag{5.10}$$

Since σ_{metals} is proportional to the metallicity:

$$\sigma_{metals}(Z) = \sigma_{metals}^{MMCC} \left(\frac{Z}{Z_\odot^{1982}} \right) \tag{5.11}$$

and thus we can compute σ_{ph} for an arbitrary metallicity.

The hydrogen ionization energy (≈ 13.6 eV) and the helium second ionization energy (≈ 54.4 eV) are much lower than the energy in play (order of keV), hence the terms σ_H and σ_{He} can be safely evaluated in Born approximation.

Following Shu 1991, the cross section in Born approximation for an hydrogen-like atom is:

$$\sigma_{Shu} = \frac{8\pi}{3\sqrt{3}} \frac{\tilde{Z}^4 m_e e^{10}}{c\hbar^3 (\hbar\omega)^3} \sqrt{\frac{48 \tilde{Z} e^2}{2 a_Z \hbar \omega}}, \tag{5.12}$$

being $\tilde{Z}$ the atomic number of each element (1 and 2 for H and He respectively),

[1] The current value for the solar metallicity is $Z_\odot = 0.0122$, from Asplund et al. 2009.

m_e and e the electron mass and charge, c the speed of light, $\hbar$ the reduced Planck constant, and $a_Z = \hbar^2/\tilde{Z} m_e e^2$.

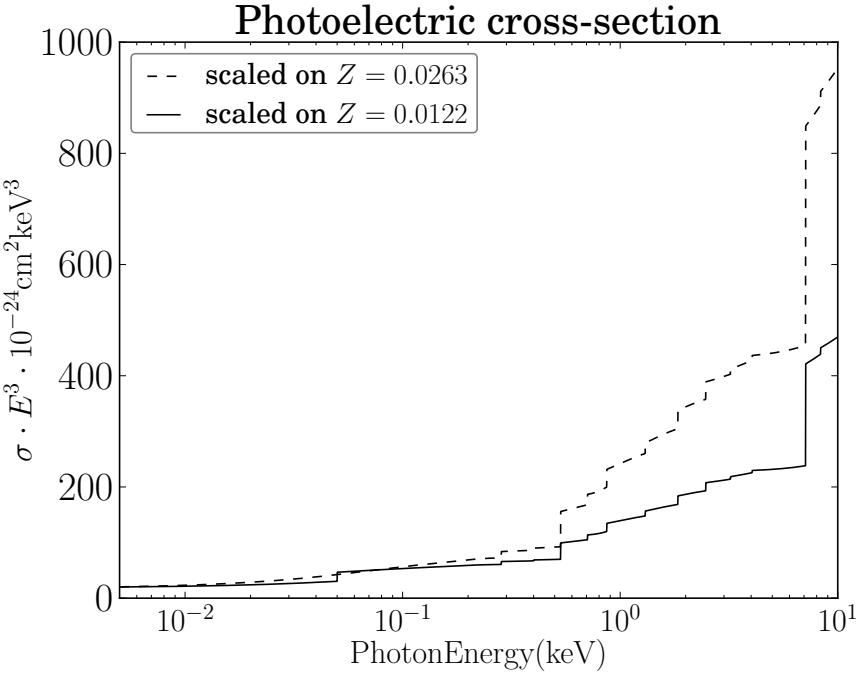

Figure 5.7: The photoelectric cross section. The dashed line shows the cross section calculated by Morrison and McCammon 1983, while the solid line represent the cross section evaluated as in equation (5.10) and scaled for solar metallicity $Z_\odot$.

Figure 5.7 shows the photoelectric cross-section calculated by Morrison and McCammon 1983 and the one evaluated with the method described above and scaled for the current solar value of the metallicity. We can highlight a few qualitative features:

- the cross section presents several gaps that corresponds to the K-shell energy of different elements. In fact in the evaluation of the photoelectric cross section has been taken into account that a certain element X contributes to the absorption only if the energy of the photons is greater than the K-shell energy. The height of the gap depends both on the abundance of the elements and on their atomic number, for example the highest gap correspond to the Fe.

- being the photoelectric cross section plotted in 5.7 multiplied by E^3, it can be evinced that the cross section is a decreasing function of the photon energy. Hence, we expect that softer X-ray photons are subjected to a heavier attenuation with respect to the harder one.

Known the cross section of the absorption processes in play, we can compute the observed flux density $F_\nu^{obs} = F_\nu e^{-\tau}$. The resulting F_ν^{obs} is shown in figure 5.8. The assumed values of the hydrogen column density and the metallicity of the system are $10^{22}\mathrm{cm}^{-2}$ and 10^{-3} respectively. The red shaded region spans over the values that the flux density takes between $\pm 3\sigma$ around the fiducial value $\alpha = 0.9$ Piconcelli et al. 2005. The attenuation is heavier in the soft X-ray band ($0.5 \div 2$keV), being about the 26% at the center of the band (1.25 keV). On the contrary, hard radiation ($2 \div 10$keV) crosses the obscuring material undergoing a very light attenuation, about the 0.1% at the center of the band (6 keV).

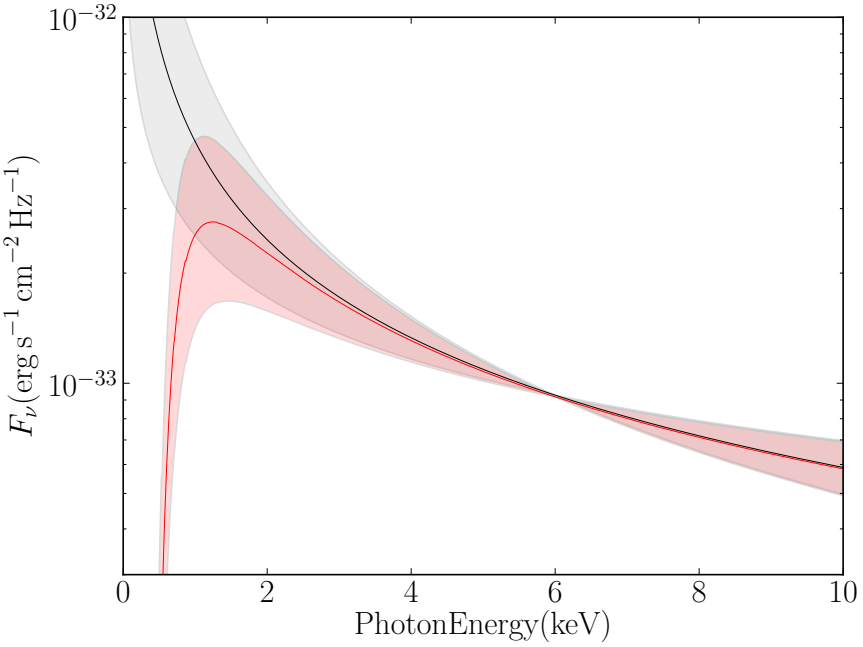

Figure 5.8: Radiative flux density of a BH accreting $1M_\odot/yr$, after the interaction (due mainly to photoelectric absorption and the Compton scattering) with the surrounding material. The assumed values of the hydrogen column density and the metallicity of the system are $10^{22}\mathrm{cm}^{-2}$ and 10^{-3} respectively. The red shaded region spans over the values that the flux density takes between $\pm 3\sigma$ around the fiducial value $\alpha = 0.9$ Piconcelli et al. 2005. The attenuation is heavier in the soft X-ray band ($0.5 \div 2$keV), being about the 26% at the center of the band (1.25 keV). On the contrary, hard radiation ($2 \div 10$keV) crosses the obscuring material undergoing a very light attenuation, about the 0.1% at the center of the band (6 keV).

Finally, figure 5.9 shows the attenuation of the intrinsic flux density of a BH accreting $1M_\odot/yr$ with a varying column density and with a metallicity value fixed on 10^{-3}.

Figure 5.10 shows the probability distribution function of the luminosity in the soft [$0.5 \div 2$keV] (dark grey) and the hard [$2 \div 10$keV] (light grey) band of the simulated progenitors for model B1, at redshifts $z = 7$, $z = 8$. The PDFs for

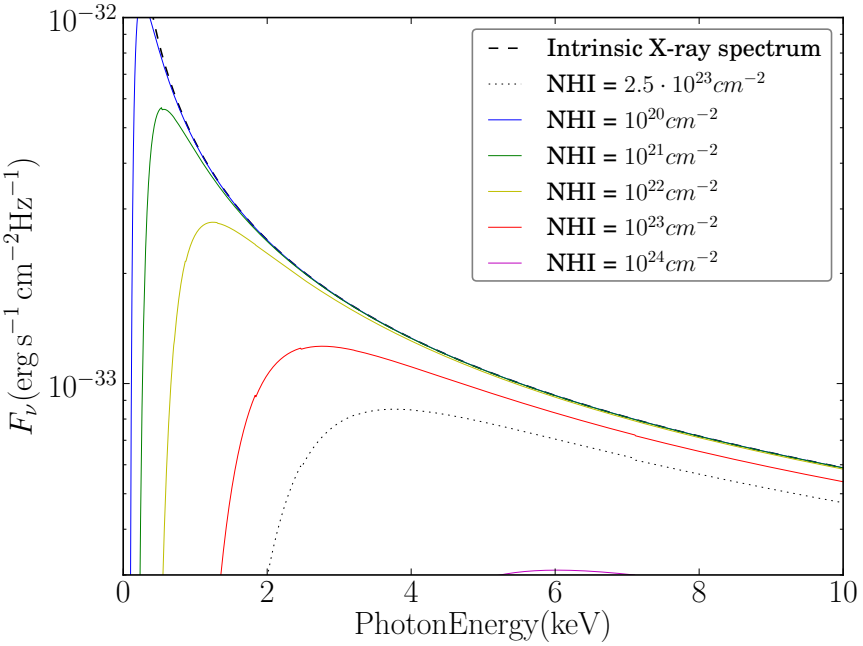

Figure 5.9: Attenuation of the intrinsic flux density of a BH accreting $1 M_\odot/yr$ as a function of N_{HI}. The assumed value of the metallicity of the system is 10^{-3}. It's worth to notice that for hydrogen column densities larger than $N_{HI} = 2.5 \times 10^{23} \mathrm{cm}^{-2}$ (dotted line) the whole emission in the soft X-ray band ($0.5 \div 2$keV) is suppressed.

model B3 present analogue features.

The PDF for the soft luminosity is shifted to lower values with respect to the hard one: this is due to the stronger attenuation of the radiation emitted by a progenitor in the soft band with respect to the hard one. To have a notion of the absorption of the soft radiation versus the absorption of the hard one, it is sufficient to give a glance at figure 5.9 and to remember that the hydrogen column densities simulated mostly belong to $10^{22}\mathrm{cm}^{-2} < \mathrm{N_{HI}} < 10^{23}\mathrm{cm}^{-2}$, so the attenuated flux density of the simulated progenitors lies, on average, between the yellow and the red lines.

Figure 5.11 shows the ratio of the soft luminosity to the hard luminosity for each progenitor (for both models and the two redshifts), quantity that hereafter will be simply called *soft to hard ratio*. As expected from previous plots and considerations, the higher is the column density, the lower is the ratio between the soft and the hard radiation that survive to the absorption.

Once highlighted the strong dependence of the soft to hard ratio on the column density, we want to understand if it has a dependence on the metallicity of the system: we considered the scatter plot of the column density and the metallicity of the system, introducing as colour the soft to hard ratio of each progenitor

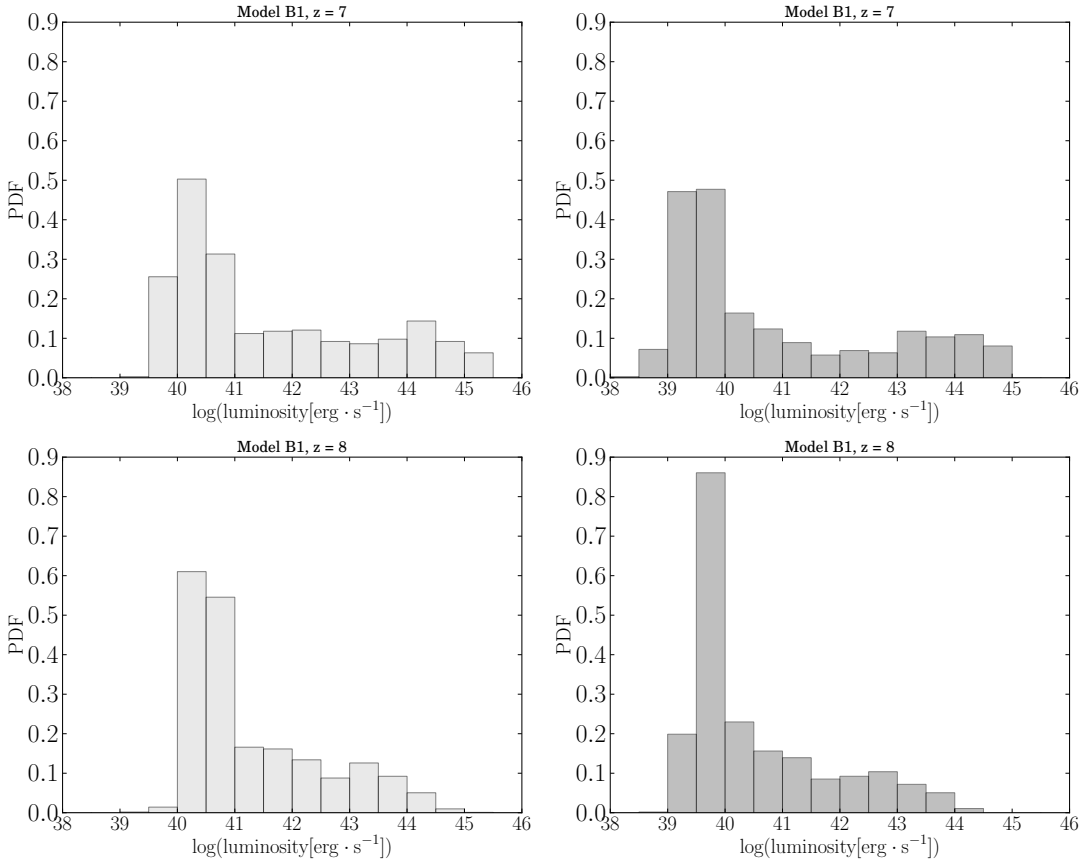

Figure 5.10: Probability distribution function of the luminosity in the soft (dark grey) and the hard (light grey) band of each simulated progenitor for the model B1, at redshifts $z = 7$, $z = 8$. As expected from figure 5.9, radiation in the soft band presents a heavier attenuation than the hard one.

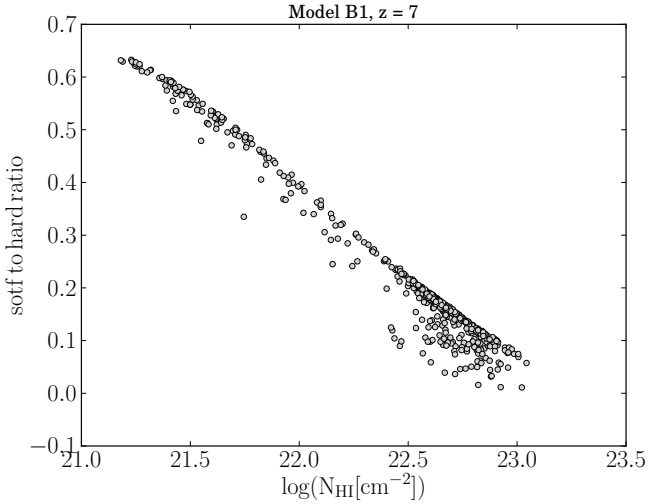

Figure 5.11: Soft to hard ratio of each simulated progenitor for model B1 at redshifts $z = 7$. As expected, the higher is the column density, the lower is the ratio between the soft and the hard radiation that survive to the absorption.

(picture 5.12).

According to picture 5.12 the soft to hard ratio depends only weakly on the metallicity of the system: the colours arrange themselves in regions that can be delimited by almost vertical lines, showing that the soft to hard ratio is mostly affected by the hydrogen column density rather than by the metallicity of the gas.

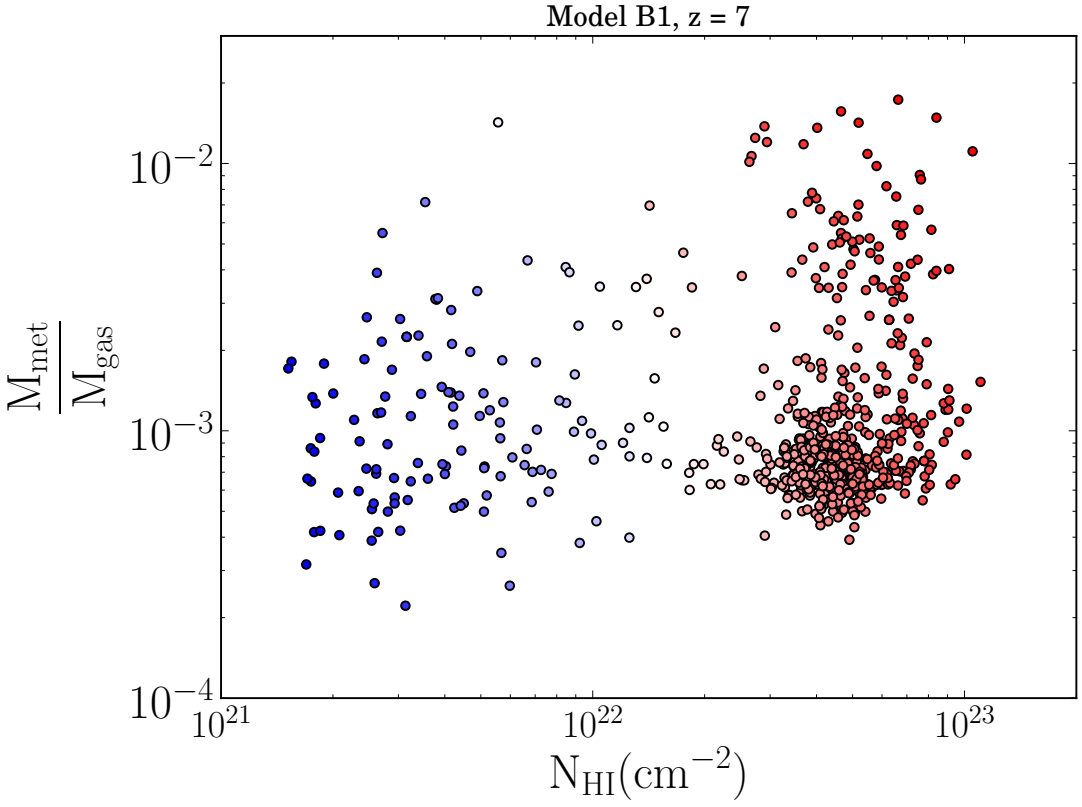

Figure 5.12: Scatter plot of the metallicity versus the hydrogen column density in which colour highlights the soft to hard ratio of each simulated progenitor: blue represents a higher value of the soft to hard ratio, while red corresponds to a lower value.

5.3.1 The dust

In the current section, evaluating the photoelectric absorption, we have totally neglected the contribution of dust.

In fact, as pointed out by Fireman 1974 the condensation of the absorbing material into grains reduces the photoelectric cross section. Morrison and McCammon 1983, following Ride and Walker 1977, estimated the importance of this effect, evaluating the photoelectric cross section in the case that all elements but H, He, Ne and Ar are totally condensed in grains (the only exception is the

oxygen that is assumed to be condensed at 25 %) : the result of their study is shown in picture 5.13; the effect is very small at low energy, where most of the absorption is due to hydrogen and helium, and at high energy, where the grains are transparent to radiation.

Because of the rather small value estimated by Morrison and McCammon 1983 for the reduction of the photoelectric cross section, the 11% just above the carbon edge (at 0.3 keV) and less than the 4% at 1 keV, we have not included the effect of grains in evaluating the absorption of the intrinsic X-ray radiation.

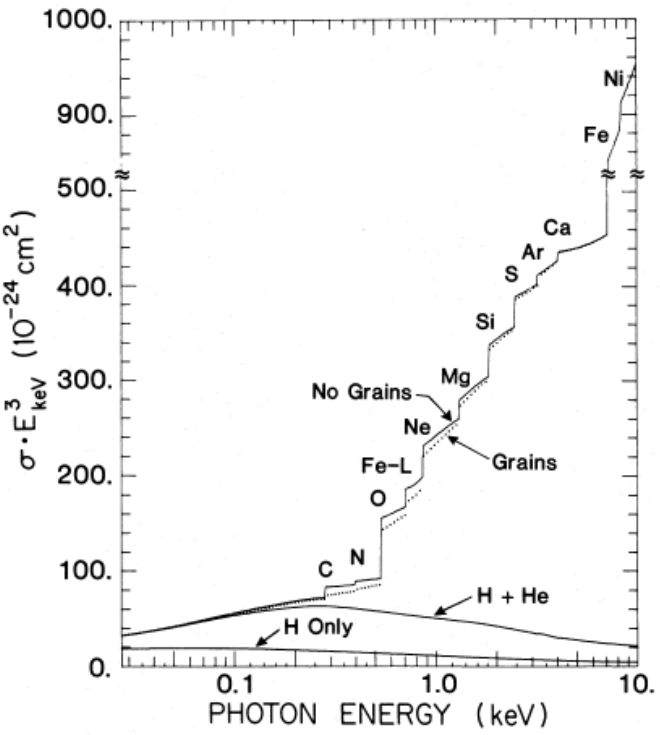

Figure 5.13: The photoelectric cross section evaluated by (Morrison and McCammon 1983). The dashed lines show the cross section calculated assuming that the 100 % of C, N, Na, Mg, Al, Si, S, Cl, Cr, Fe, Ni and the 25% of O are condensed into grains. With courtesy of (Morrison and McCammon 1983).

6 Observational forecasts

In the last chapter we modelled the X-ray emission of an accreting black hole taking into account the absorption from the obscuring material in the black hole environs.

In this final chapter we will try to understand if the SMBHs' ancestors predicted by theoretical models, but never detected so far, are indeed too faint (sec. 6.1) or too rare (sec. 6.2) to be detected with the current observational tools; we will focus on the most powerful observatory at the moment: the Chandra X-ray Observatory.

In section 6.1, we will describe the main observational features (such as the sensitivity, the energy bandpass and the field of view) of the Chandra X-ray observatory. In section 6.2 we will calculate the expected number of detectable progenitors as a function of the characteristics of the performed survey and in section 6.3 we will propose an observational strategy in order to maximize the probability to detect a supermassive black holes' progenitor.

6.1 The sensitivity of Chandra

The Chandra X-ray Observatory was launched in 1999 and it is still in operation. The telescope consists in the High Resolution Mirror Assembly (HRMA) that is large 1.2 meters and has an effective collection area of 400 cm^2 at 1 keV. The extreme accuracy of HMRA permits an angular resolution unprecedented for this kind of instruments: 0.5 arcsec.

Chandra has multiple focal plane instruments but in this work we will use only the Advanced CCD Imaging Spectrometer (ACIS): it collects photons in an energy range of $\Delta E = 0.5 \div 8$keV, divided in a soft ($\Delta E_{soft} = 0.5 \div 2$keV) and a hard band ($\Delta E_{hard} = 2 \div 8\,$keV). In the imaging setup the ACIS has four CCD chips each one with 1024x1024 pixels and an image scale of 0.5 arcsec per pixel; this results in a field of view of 16.9x16.9 $arcmin^2$.

Since we are interested in high-redshift signals, the observational Chandra energy bands ΔE_{soft} and ΔE_{hard} in the rest frame are multiplied by $(1 + z)$. So

that at redshift $z = 7$, ΔE_{soft} corresponds to a energy range of $[4, 16]$ keV in the rest frame of the source that we want to detect. For this reason we can see that even the soft Chandra energy band is dominated by the hard component of the X-ray spectrum of the source.

In the following we will need to compute the Chandra sensitivity (i.e. the minimum detectable flux) for an arbitrary exposure time; in general in an instrument we can have two types of noise:

- the detector noise: since this component adds a number of electrons in each pixel with a time independent variance, its weight scales as the inverse of time
$$\sigma(t) \propto t^{-1} \tag{6.1}$$

- the background noise: this noise arises from the Poisson fluctuations in the number of the background photons. Since the variance of the number of electrons that corresponds to this noise increases with the square root of the exposure time, we have

$$\sigma(t) \propto t^{-1/2} \tag{6.2}$$

In general it is not trivial to determine which one of the two noise components dominates; in fact this depends on the background intensity; we expected that for large enough exposure time the second one dominates, but the calculation of the threshold is beyond the aim of this work.

We adopted an empirical approach: from Xue et al. 2011, Alexander et al. 2003, Elvis et al. 2009 and Lehmer et al. 2005 we know the sensitivity of Chandra in both the hard and the soft band if it performs observations with exposure time of 4 Ms, 2 Ms, 0.16 Ms and 0.25 Ms, respectively.

Figure 6.1 show that, in both the hard and the soft band of Chandra, these values can be well fitted by a $1/t$ law, where t is the exposure time. Therefore we can conclude that for exposure time smaller than 4 Ms Chandra is not background limited and:

$$\sigma(t) = 10^{-16.45} \frac{1\text{Ms}}{t} \text{erg} \cdot \text{s}^{-1} \cdot \text{cm}^{-2} \tag{6.3}$$

for the Chandra soft band,

$$\sigma(t) = 10^{-15.73} \frac{1\text{Ms}}{t} \text{erg} \cdot \text{s}^{-1} \cdot \text{cm}^{-2} \tag{6.4}$$

for the Chandra hard band.

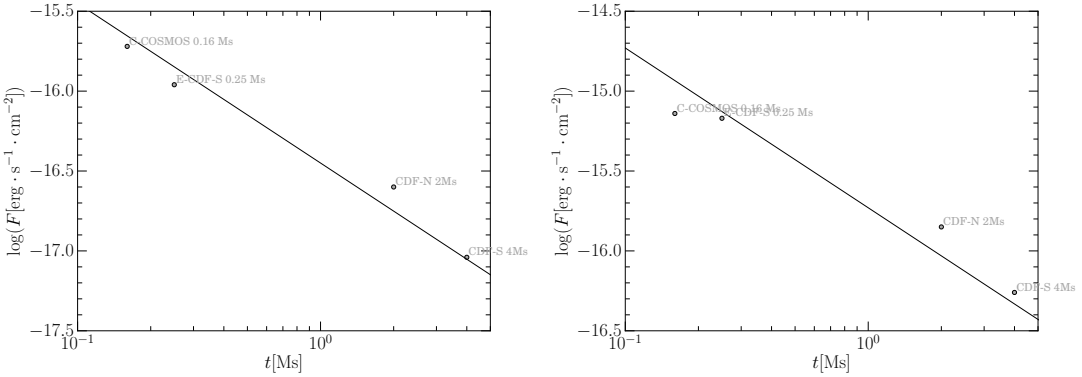

(a) Chandra soft band ([0.5, 2] keV) **(b)** Chandra hard band ([2,8] keV)

Figure 6.1: Sensitivity of Chandra Space Telescope. The values of the sensitivity from Xue et al. 2011, Alexander et al. 2003, Elvis et al. 2009 and Lehmer et al. 2005 are fitted with: $\sigma(t) = 10^{-16.45}\frac{1\mathrm{Ms}}{t}\mathrm{erg}\cdot\mathrm{s}^{-1}\cdot\mathrm{cm}^{-2}$ and $\sigma(t) = 10^{-15.73}\frac{1\mathrm{Ms}}{t}\mathrm{erg}\cdot\mathrm{s}^{-1}\cdot\mathrm{cm}^{-2}$ in the Chandra soft and hard band respectively. Since the instrument has a higher sensitivity in the soft band than in the hard one, it is more advantageous to look for faint objects in this band.

We want to understand if the current Chandra surveys can detect the faint progenitors of luminous quasars once we assume that their emission is the one predicted in chapter 5, starting from the progenitors simulated by Valiante et al. 2011.

To do so, we integrated the spectral energy distribution F_ν^{obs} (eq.(5.7)) in the Chandra soft band $\Delta E_{soft} = [0.5, 2]$ keV, that corresponds to $\Delta E_{soft}^{z=7} = [4, 16]$ keV and $\Delta E_{soft}^{z=8} = [4.5, 18]$ keV for sources at $z = 7$ and $z = 8$, respectively.

Figure 6.2 shows the PDF of the expected flux of the supermassive black holes' progenitors at redshift $z = 7$ and $z = 8$ in the Chandra soft band: the vertical lines show the minimum flux detectable by Chandra with exposure time of 4 Ms, 1 Ms and 0.01 Ms.

Similarly, if we are interested in the Chandra hard band $\Delta E_{hard} = [2, 8]$ keV, that corresponds to $\Delta E_{hard}^{z=7} = [16, 64]$ keV and $\Delta E_{hard}^{z=8} = [18, 72]$ keV for sources at $z = 7$ and $z = 8$, respectively Figure 6.3 shows the PDF of the expected flux of the SMBHs' progenitors at $z = 7$ and $z = 8$ in the hard Chandra band.

Accordingly to fig. 6.2 and 6.3 we have the possibility to observe the most luminous part of the progenitors with the Chandra X-ray Observatory: hence, in the next section we will explore the possibility that these sources have not been observed so far because they are rare.

Since from a comparison between fig. 6.2 and 6.3 we see that there are not remarkable differences in the expected flux (and so in the observational forecasts) but the sensitivity of the instrument in the hard band is lower: hence, hereafter, we will only show the details for the detection of the SMBHs' ancestors using the

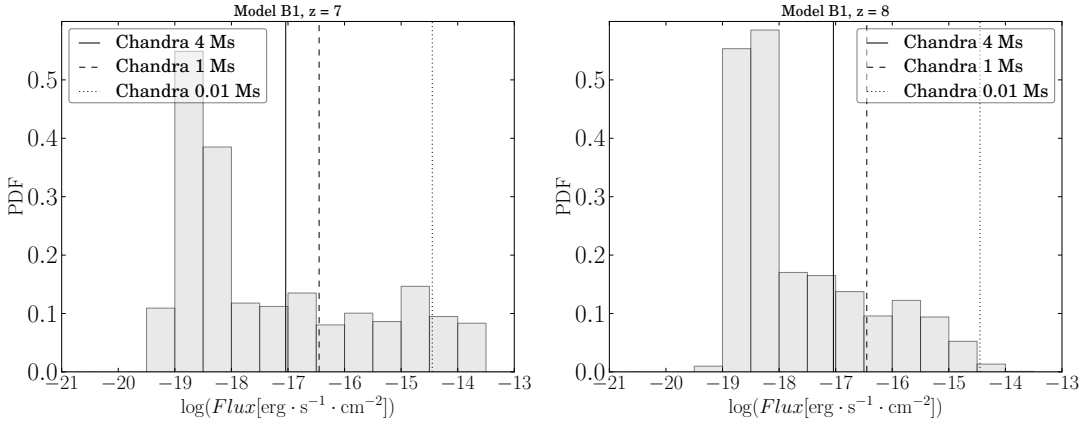

Figure 6.2: PDF of the expected flux in the Chandra soft band at redshift $z = 7$ (a) and $z = 8$ (b): the vertical lines show the minimum flux detectable by Chandra with exposure time of 4 Ms, 1 Ms and 0.01 Ms.

Chandra soft energy band.

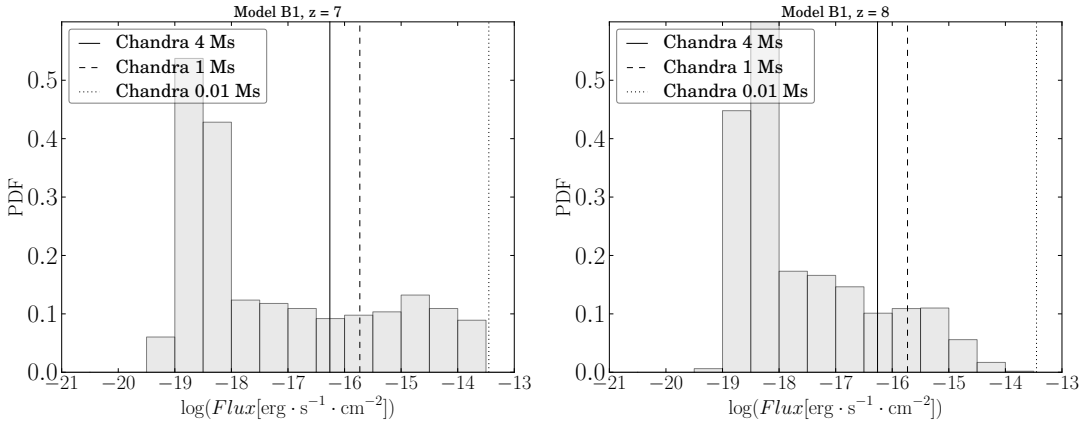

Figure 6.3: PDF of the expected flux in the Chandra soft band at redshift $z = 7$ (a) and $z = 8$ (b): the vertical lines show the minimum flux detectable by Chandra with exposure time of 4 Ms, 1 Ms and 0.01 Ms.

6.2 Statistical analysis

Since the progenitors simulated by Valiante et al. 2011 have been created in order to reconstruct the merger history of a dark matter halo of mass $10^{13} M_{\odot}$ at $z = 6.4$, we can evaluate the comoving volume in which the simulated progenitors are scattered as the ratio of the halo mass to the average comoving density of the universe, $\rho_c = \frac{3H^2}{8\pi G} \approx 10^{-29}\mathrm{cm}^{-3}$. This way, the volume[1] of one Valiante et al. 2011 box is $V_{box} = 79\mathrm{cMpc}^3$.

[1]We have chosen to use comoving units, because they are redshift independent

For our purpose, we will assume that the simulated progenitors lie on the two-dimensional surface $S_{box} = V^{2/3} = 18.38\text{cMpc}^2$, corresponding to a square of side $L_{box} = V^{1/3} = 4.28\text{cMpc}$. At redshift $z = 7$, the surface S_{box} corresponds to $\approx 1.7\,\text{x}\,1.7\text{arcmin}^2$, much smaller than the field of view (FOV) of Chandra $A_{Chandra} = 16.9\,\text{x}\,16.9\text{arcmin}^2$.

Anyway, according to the Sheth and Tormen (ST) mass function (Sheth and Tormen 1999), at $z = 6.4$ we are supposed to find on average 0.2 halos of $10^{13} M_\odot$ every Gpc^3. Thus, in volume of 5 Gpc^3 we find one Valiante's box on average. The volume of 5 Gpc^3 corresponds to a bidimensional surface $\approx 700 \times 700\,\text{arcmin}^2$, that can be completely explored by a survey that performs an observation that covers about 4×10^5 pointings with the FOV of Chandra; anyway this observation would be really challenging, because of the time needed to perform a so high number of pointings.

The number of progenitors N expected to be observed by a survey that has a sensitivity equal to F and that probes an area A of the sky is:

$$N(F, A) = \bar{N}(F)\frac{A}{A_{ST}}, \tag{6.5}$$

where, $\bar{N}(F)$ is the number of progenitors that have a flux sufficient to be detected by an instrument of sensitivity F, A is the area explored by the survey and A_{ST} is the area corresponding to the volume occupied by one Valiante et al. 2011 box according to the Sheth and Tormen mass function $(5\text{Gpc}^3)^{2/3}$.

Figure 6.4 shows $N(F, A)$ estimated with model B1 of Valiante et al. 2011 data, at $z = 7$ and $z = 8$. The slope of the lines with the same colour (i.e. the same value of $N(F, A)$) is much steeper at $z = 7$ that at $z = 8$: in fact, with increasing redshift the progenitors are more numerous (and smaller) so the same increase in A corresponds to a larger increase in the detectable progenitors at $z = 8$. Blue points correspond to actual Chandra surveys, whose characteristics are examined in depth in Xue et al. 2011, Alexander et al. 2003, Elvis et al. 2009 and Lehmer et al. 2005 . The meaning of the red points will be explained in sec. 6.3; we will see that they correspond to the estimated best observational strategy for a given exposure time. The position of the points in the $F-A$ plane implies that the most sensitive survey performed nowadays, the Chandra Deep Field-South (CDF-S), that have a total effective time exposure of 4 Ms and explores a solid angle of 465 arcmin^2, is observationally disadvantaged with respect to the Chandra COSMOS (C-COSMOS) that, having effective exposure of 0.16 Ms, is much less sensitive but cover a much wider region of the sky (6120 arcmin^2). Hence, to improve

the probability to detect a SMBH ancestor it seems to be observationally more advantageous to perform several pointings than to increase the sensitivity with a higher exposure time for a single pointing. This statement will be confirmed and studied in detail in the next chapter.

6.3 Best observational strategy

In this section, we will try to understand if it is more observational advantageous to increase the survey sensitivity or increase the area of the sky probed by the survey. To do so, we will suppose to perform an imaginary experiment, in which we have the Chandra space telescope available for a determined time T_{tot}; it is interesting to calculate how invest this time in order to get the maximum probability to detect one of the objects that we are looking for.

As representative set, we choose to focus on the results from the analysis of the B1 set of Valiante's data. The total time required by a Chandra survey that probe an area A of the sky, executing $n = A/A_{Chandra}$ pointings, each one with an exposure time t_{exp}, is:

$$T_{tot} = T_{eff} + \zeta \frac{A}{A_{Chandra}} \tag{6.6}$$

where the effective time

$$T_{eff} = t_{exp} \frac{A}{A_{Chandra}} \tag{6.7}$$

takes into account that some of the time is wasted in technical operations needed to move the telescope in order to probe different regions of the sky. According to Elvis et al. 2009, the Chandra COSMOS survey performed four exposure with nominal total exposure time $T_{tot} = 0.20$ Ms and effective exposure time $T_{eff} = 0.16$ Ms; hence, the technical time needed to prepare the telescope for a pointing in a region of the sky is estimated to be $\zeta = 0.01$ Ms.

Once we keep T_{tot} fixed, we can exploit eqs. (6.5) and (6.7) exploring the parameter space in search of the values of the sensitivity F and the covered area A to maximize the detectable number of progenitors.

Having followed this procedure for several values of the available time T_{tot}, we obtained a plot (figure 6.5) of the maximum number of $z = 7, 8$ detectable progenitors as a function of the time available for the observation, according to our emission model developed in chapter 5. The observational forecast is slightly more optimistic (with N_{max} the 20% higher at $T_{tot} = 4$Ms) if the estimate is done

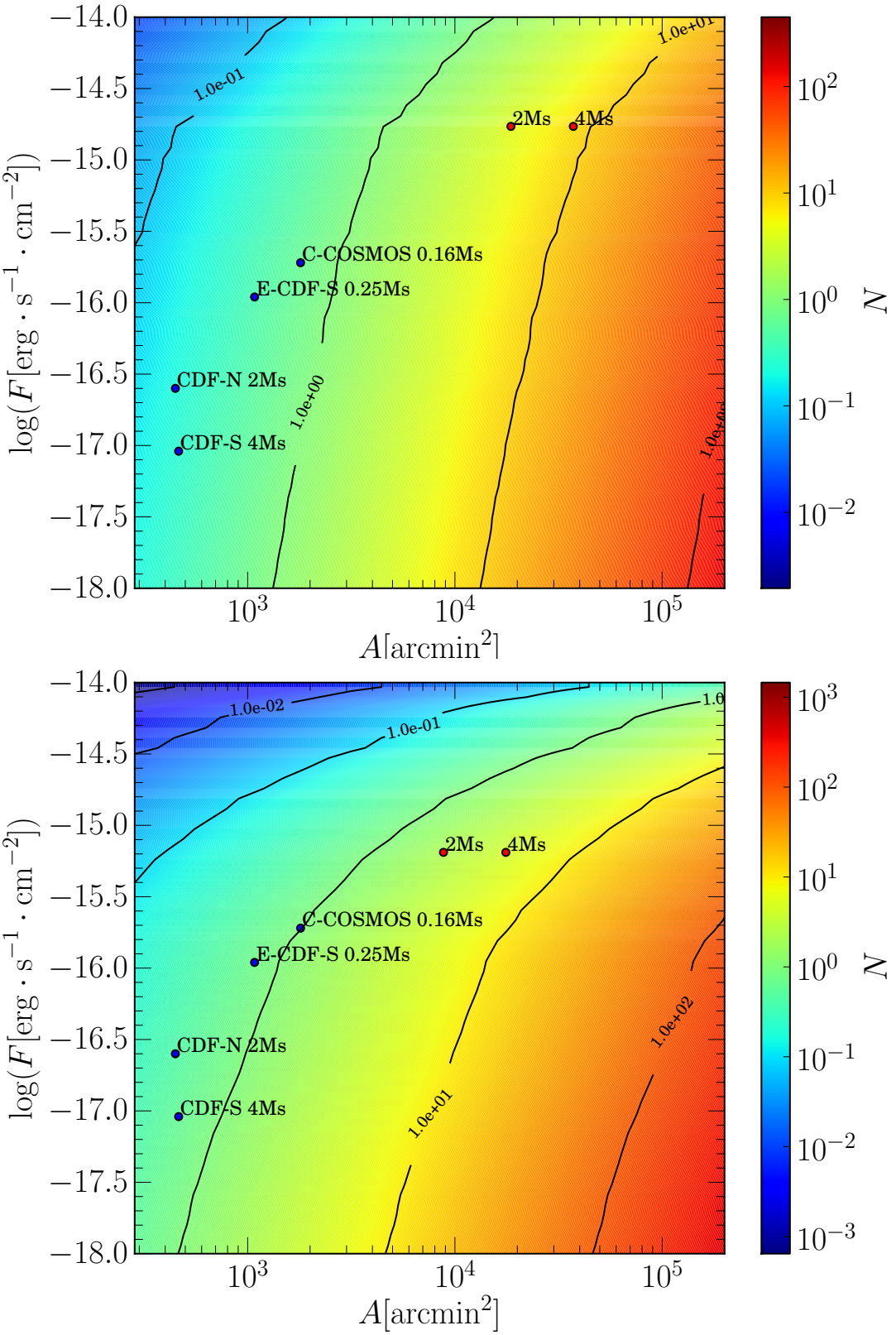

Figure 6.4: Progenitors expected to be detect with the current Chandra surveys (blue points) according to our emission model. The upper(lower) panel corresponds to the observational forecasts at $z = 7(z = 8)$. According to the figure, less sensitive but wider surveys such as C-COSMOS 0.16 Ms are observatively advantageous with respect to deeper but narrower ones (such as the CDF-S) Red points refers to imaginary surveys that maximize the probability to detect a progenitors once we assign an observation time (here, 2 Ms and 4 Ms).

considering the progenitors simulated by Valiante et al. 2011 according to their model B1, but totally analogue to the ones from model B3.

It is worth to notice that this result depends strongly on the parameter ζ: we estimated that if it was ten times greater, in 4 Ms the maximum number of detectable progenitors at $z = 7$ would be almost three times lower.

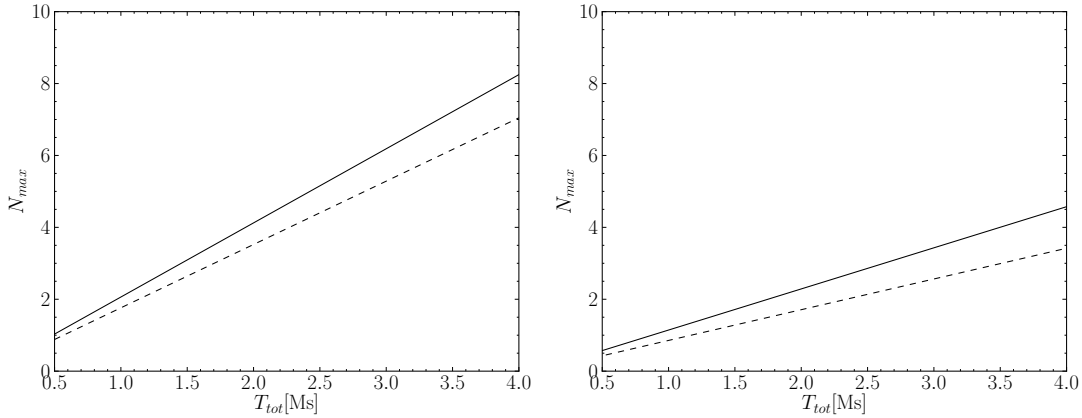

(a) $z = 7$ **(b)** $z = 8$

Figure 6.5: Maximum number of $z = 7$, $z = 8$ ((a) and (b), respectively) progenitors detectable by the Chandra space telescope in a total exposure time T_{tot}. The solid (dashed) line corresponds to the model B1 (B3) by Valiante et al. 2011 : the observational forecast is more optimistic in model B1.

After these considerations, we can go back to figure 6.4. The red points in the picture represent the values of the sensitivity and the covered area that maximize the probability to detect a progenitor in an imaginary survey that observe the sky for an efficient time of 2 Ms and 4 Ms. It is clear from the arrangement of the these points in the $F - A$ plane with respect to the actual CDF-N (2Ms) and CDF-S (4Ms) that observatively is more advantageous to enlarge the probed area rather than increase the sensitivity.

Because of the rarity of the expected progenitors, a shallow but large survey have more chances to detect them with respect to a deeper but narrower one. Anyway, being the ancestors at $z = 8$ fainter than their "sons" at $z = 7$, they need deeper surveys to be detected as we can see by the comparison between the two pictures of fig.6.4.

To conclude this section, it's important to discuss the validity of the prediction of this thesis about the detectable MBHs ancestors. Being sprang from the study of a very special region (the volume simulated by Valiante et al. 2011), our estimate of the number of detectable progenitors is just a lower bound: according to the ST mass function, in 5Gpc^3 we are supposed to find only one Valiante's box (in which the progenitors of a quasar at $z = 6.4$ are scattered), but, in principle,

we cannot rule out the possibility to find in this volume progenitors of quasars that are going to form at later times or intermediate mass BHs that are not going to form any quasar.

From this work we can highlight a few important points:

- SMBHs' ancestors are luminous enough to be detected in the X-ray band by Chandra. In fact, being settled at high redshift, even the Chandra soft energy bandpass corresponds to rest frame energies that are hard enough to be unobscured.

- These objects are extremely rare. None of the surveys performed so far probes a region of the sky large enough for the detection to be statistically probable.

- The best observational strategy fixes the sensitivity of the survey to a value sufficient to detect the outliers and explores an area large enough to make the detection statistically probable.

Therefore, even if SMBHs' ancestors have not been detected so far, we expect the detection to be possible in the near future. Obviously we will need more in-depth studies with more realistic models, but the results of this work encourage new surveys.

7 Conclusions

In this work we modelled the X-ray emissivity of supermassive black holes (SMBH) ancestors. In particular we studied the spectrum of their emission and the feasibility of surveys with an high detection probability.

The scientific issue related to the supermassive black holes (SMBHs) formation is still outstanding: indeed observers found SMBHs with $M > 10^9 M_\odot$ less than a Gyr after the Big Bang. These observations are very challenging for our theoretical models and the formation mechanisms of these objects is still an open problem. In fact, we expect that SMBHs' ancestors are present at higher redshift but they have never been observed so far. Their detection would be an important breakthrough that would allow us to reach a deeper knowledge on these mysterious and problematic objects. Several attempts have been done in oder to reveal them but, so far, there have not been positive responses.

This work investigated the ancestors visibility the X-ray band: indeed, black holes are characterized by a very hard spectrum and a strong X-ray emission; this could be used to discriminate them from "ordinary" galaxies, powered by stars. To do so, we followed two steps:

- we developed a model for the progenitors' X-ray flux: according to the observations of low-redshift quasars, the intrinsic flux has been modeled as a single power-law in the energy range [0.5-10] keV.

- We exploited the results of a semi-numerical simulation, that provides details on the progenitors accretion and on the amount of obscuring material in their environs, to evaluate the X-ray emission of the progenitors. In the evaluation of the expected flux, several attenuation mechanisms have been taken into account, finding that the dominant one is the interstellar photoelectric absorption within the host galaxy.

As a result, we found that the predicted X-ray flux is highly suppressed in the soft band ($[0.5 \div 2]$ keV), almost unobscured in the hard one ($[2 \div 10]$ keV). Interestingly, we found that the most luminous SMBHs ancestors are very bright and

well in reach of the most powerful current observatories. Hence, we investigated the reasons for the non-detection.

We developed a statistical analysis in order to compute the volume density of these objects. We found that this negative response is due to the rarity of these sources and to the limited area probed by the latest deep surveys: therefore the non-detection is statistically expected.

To examine in depth this issue, in the final part of the thesis:

- We developed a formalism to obtain, given the characteristics of the survey, how many sources are supposed to be detected. As expected for the rarity of these objects, none of the surveys performed so far probes a region of the sky large enough for the detection to be statistically probable.

- We planned the best observational strategy, finding out that is more advantageous for a survey to explore an area as large as possible to the detriment of the sensitivity. The results are encouraging because none of the past surveys implemented the optimal strategy and therefore there is ample room for improvement.

The conclusion of this work are very exciting: indeed, the detection of SMBHs' ancestors is already at reach of our observational capabilities. Therefore, even if they have not been detected so far, we expect the detection to be possible in the near future; this will be a milestone in the SMBHs observational history, leading to binding constraints in our theoretical models. Obviously we will need more in-depth studies with more realistic models, but we hope that the results of this work will encourage new studies and new surveys in search of these fascinating objects.

Bibliography

Alexander, D. M. et al. (Aug. 2003). "The Chandra Deep Field North Survey. XIII. 2 Ms Point-Source Catalogs". In: *AJ* 126, pp. 539–574. DOI: 10.1086/376473. eprint: astro-ph/0304392.

Asplund, M. et al. (Sept. 2009). "The Chemical Composition of the Sun". In: *ARAA* 47, pp. 481–522. DOI: 10.1146/annurev.astro.46.060407.145222. arXiv:0909.0948 [astro-ph.SR].

Berti, E., V. Cardoso, and C. M. Will (Mar. 2006). "Gravitational-wave spectroscopy of massive black holes with the space interferometer LISA". In: *PhysRevD* 73.6, 064030, p. 064030. DOI: 10.1103/PhysRevD.73.064030. eprint: gr-qc/0512160.

Bromm, V. and A. Loeb (Oct. 2003). "Formation of the First Supermassive Black Holes". In: *ApJ* 596, pp. 34–46. DOI: 10.1086/377529. eprint: astro-ph/0212400.

Carr, B. J., J. R. Bond, and W. D. Arnett (Feb. 1984). "Cosmological consequences of Population III stars". In: *ApJ* 277, pp. 445–469. DOI: 10.1086/161713.

Carroll, S. M., W. H. Press, and E. L. Turner (1992). "The cosmological constant". In: *ARAA* 30, pp. 499–542. DOI: 10.1146/annurev.aa.30.090192.002435.

Comastri, A. (Aug. 2004). "Compton-Thick AGN: The Dark Side of the X-Ray Background". In: *Supermassive Black Holes in the Distant Universe*. Ed. by A. J. Barger. Vol. 308. Astrophysics and Space Science Library, p. 245. eprint: astro-ph/0403693.

Eisenstein, D. J. and W. Hu (Mar. 1998). "Baryonic Features in the Matter Transfer Function". In: *ApJ* 496, pp. 605–614. DOI: 10.1086/305424. eprint: astro-ph/9709112.

Elvis, M. et al. (Sept. 2009). "The Chandra COSMOS Survey. I. Overview and Point Source Catalog". In: *ApJS* 184, pp. 158–171. DOI: 10.1088/0067-0049/184/1/158. arXiv:0903.2062 [astro-ph.CO].

Fireman, E. L. (Jan. 1974). "Interstellar Absorption of X-Rays". In: *ApJ* 187, pp. 57–60. DOI: 10.1086/152588.

Frank, J., A. King, and D. Raine (2002). *Accretion Power in Astrophysics*. Cambridge University Press. ISBN: 9780521629577. URL: https://books.google.it/books?id=GGM_t-xn8ocC.

Greif, T. H. et al. (Aug. 2011). "Simulations on a Moving Mesh: The Clustered Formation of Population III Protostars". In: *ApJ* 737, 75, p. 75. DOI: 10.1088/0004-637X/737/2/75. arXiv:1101.5491.

Lacey, C. and S. Cole (June 1993). "Merger rates in hierarchical models of galaxy formation". In: *MNRAS* 262, pp. 627–649.

Larson, R. B. (Dec. 1998). "Early star formation and the evolution of the stellar initial mass function in galaxies". In: *MNRAS* 301, pp. 569–581. DOI: 10.1046/j.1365-8711.1998.02045.x. eprint: astro-ph/9808145.

Lehmer, B. D. et al. (Nov. 2005). "The Extended Chandra Deep Field-South Survey: Chandra Point-Source Catalogs". In: *ApJS* 161, pp. 21–40. DOI: 10.1086/444590. eprint: astro-ph/0506607.

Marconi, A. et al. (June 2004). "Local supermassive black holes, relics of active galactic nuclei and the X-ray background". In: *MNRAS* 351, pp. 169–185. DOI: 10.1111/j.1365-2966.2004.07765.x. eprint: astro-ph/0311619.

Morrison, R. and D. McCammon (July 1983). "Interstellar photoelectric absorption cross sections, 0.03-10 keV". In: *ApJ* 270, pp. 119–122. DOI: 10.1086/161102.

Mortlock, D. J. et al. (June 2011). "A luminous quasar at a redshift of z = 7.085". In: *Nature* 474, pp. 616–619. DOI: 10.1038/nature10159. arXiv:1106.6088 [astro-ph.CO].

Netzer, Hagai (2013). "The physics and evolution of active galactic nuclei". In:

Omukai, K., R. Schneider, and Z. Haiman (Oct. 2008). "Can Supermassive Black Holes Form in Metal-enriched High-Redshift Protogalaxies?" In: *ApJ* 686, pp. 801–814. DOI: 10.1086/591636. arXiv:0804.3141.

Padmanabhan, T. (1993). *Structure Formation in the Universe*. Cambridge University Press.

Petri, A., A. Ferrara, and R. Salvaterra (May 2012). "Supermassive black hole ancestors". In: *MNRAS* 422, pp. 1690–1699. DOI: 10.1111/j.1365-2966.2012.20743.x. arXiv:1202.3141 [astro-ph.CO].

Piconcelli, E. et al. (Mar. 2005). "The XMM-Newton view of PG quasars. I. X-ray continuum and absorption". In: *A&A* 432, pp. 15–30. DOI: 10.1051/0004-6361:20041621. eprint: astro-ph/0411051.

Planck Collaboration et al. (Feb. 2015). "Planck 2015 results. XIII. Cosmological parameters". In: *ArXiv e-prints*. arXiv:1502.01589.

Press, W. H. and P. Schechter (Feb. 1974). "Formation of Galaxies and Clusters of Galaxies by Self-Similar Gravitational Condensation". In: *ApJ* 187, pp. 425–438. DOI: 10.1086/152650.

Ride, S. K. and A. B. C. Walker Jr. (Nov. 1977). "Absorption of X-rays in the interstellar medium". In: *A&A* 61, pp. 339–346.

Romero, G.E. and G.S. Vila (2013). *Introduction to Black Hole Astrophysics*. Lecture Notes in Physics. Springer Berlin Heidelberg. ISBN: 9783642395963. URL: https://books.google.it/books?id=sCm6BQAAQBAJ.

Salpeter, E. E. (Jan. 1955). "The Luminosity Function and Stellar Evolution." In: *ApJ* 121, p. 161. DOI: 10.1086/145971.

Schutz, B.F. (1985). *A First Course in General Relativity*. Series in physics. Cambridge University Press. ISBN: 9780521277037. URL: https://books.google.it/books?id=qhDFuWbLlgQC.

Shapiro, S. L. (Mar. 1973). "Accretion onto Black Holes: the Emergent Radiation Spectrum". In: *ApJ* 180, pp. 531–546. DOI: 10.1086/151982.

Sheth, R. K. and G. Tormen (Sept. 1999). "Large-scale bias and the peak background split". In: *MNRAS* 308, pp. 119–126. DOI: 10.1046/j.1365-8711.1999.02692.x. eprint: astro-ph/9901122.

Shu, Frank H. (1991). "The Physics of Astrophysics: Radiation". In:

Sobral, D. et al. (Aug. 2015). "Evidence for PopIII-like Stellar Populations in the Most Luminous Lyman-alpha Emitters at the Epoch of Reionization: Spectroscopic Confirmation". In: *ApJ* 808, 139, p. 139. DOI: 10.1088/0004-637X/808/2/139. arXiv:1504.01734.

Thorne, K. S. (July 1974). "Disk-Accretion onto a Black Hole. II. Evolution of the Hole". In: *ApJ* 191, pp. 507–520. DOI: 10.1086/152991.

Valiante, R. et al. (Sept. 2011). "The origin of the dust in high-redshift quasars: the case of SDSS J1148+5251". In: *MNRAS* 416, pp. 1916–1935. DOI: 10.1111/j.1365-2966.2011.19168.x. arXiv:1106.1418.

Vietri, M. (2006). *Astrofisica delle alte energie*. Programma di matematica, fisica, elettronica. Bollati Boringhieri. ISBN: 9788833957739. URL: https://books.google.it/books?id=Qd5tAAAACAAJ.

Volonteri, M. (July 2010). "Formation of supermassive black holes". In: *A&ARv* 18, pp. 279–315. DOI: 10.1007/s00159-010-0029-x. arXiv:1003.4404.

Volonteri, M. and D. P. Stark (Nov. 2011). "Assessing the redshift evolution of massive black holes and their hosts". In: *MNRAS* 417, pp. 2085–2093. DOI: 10.1111/j.1365-2966.2011.19391.x. arXiv:1107.1946.

Willott, C. J., R. J. McLure, and M. J. Jarvis (Apr. 2003). "A $3\times10^9 M_\odot$ Black Hole in the Quasar SDSS J1148+5251 at z=6.41". In: *ApJL* 587, pp. L15–L18. DOI: 10.1086/375126. eprint: astro-ph/0303062.

Willott, C. J. et al. (Aug. 2010). "Eddington-limited Accretion and the Black Hole Mass Function at Redshift 6". In: *AJ* 140, pp. 546–560. DOI: 10.1088/0004-6256/140/2/546. arXiv:1006.1342.

Xue, Y. Q. et al. (July 2011). "The Chandra Deep Field-South Survey: 4 Ms Source Catalogs". In: *ApJS* 195, 10, p. 10. DOI: 10.1088/0067-0049/195/1/10. arXiv:1105.5643.

Yaqoob, T. (Apr. 1997). "X-Ray Transmission in Cold Matter: Nonrelativistic Corrections for Compton Scattering". In: *ApJ* 479, pp. 184–189.